

**Volumetric Quantitative Analysis of Receptor Function**

by

**Kelly E. Canales**

**B.S., Physics  
University of Chicago (1992)  
M.S., Applied Mathematics  
Northwestern University (1995)**

**Submitted to the Department of Mechanical Engineering in Partial  
Fulfillment of the Requirements for the Degree of  
Master of Science in Mechanical Engineering**

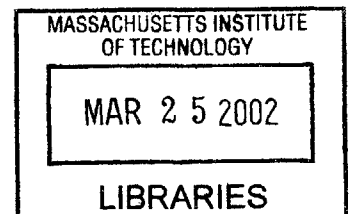
at the

**Massachusetts Institute of Technology**

**February 2002**

**© 2002 Massachusetts Institute of Technology  
All rights reserved**

**BARKER**



**Signature of Author** \_\_\_\_\_

**Department of Mechanical Engineering  
January 18, 2002**

**Certified By** \_\_\_\_\_

**Anna-Liisa Brownell  
Associate Professor, Department of Radiology, Harvard Medical School  
Thesis Supervisor**

**Certified By** \_\_\_\_\_

**Derek Rowell  
Professor, Department of Mechanical Engineering, MIT  
Thesis Supervisor**

**Accepted By** \_\_\_\_\_

**Ain Sonin  
Chairman, Department Committee on Graduate Students**

# Volumetric Quantitative Analysis of Receptor Function, Oxidative Metabolism, and Glucose Metabolism

by

Kelly E. Canales

Submitted to the Department of Mechanical Engineering on January 18, 2002 in partial fulfillment of the requirements for the Degree of Master of Science in Mechanical Engineering

## ABSTRACT

In neurological disorders such as Parkinson's disease, examination of the living brain by high-resolution positron emission tomography (PET), combined with the appropriate pharmacokinetic and physiological analyses, can provide valuable quantitative information of altered brain function. The primary objective of the thesis is accomplished by developing a volumetric process for the quantitative analysis of receptor function in a primate model of Parkinson's disease. This method of analysis can be used to more accurately quantify the neuropathological and neurochemical alterations observed in Parkinson's disease and can thus be used to gain a greater understanding of the disease.

Fusion of PET images and magnetic resonance (MR) images provides the necessary step for combining the functional information obtained from PET with the anatomical information obtained from MR. The benefit of having fused images is that it enables the visualization of functional PET data by superimposing it on a high-resolution anatomical MR image and therefore improves localization of radioligand-receptor binding and metabolic activity in the brain. When the living brain is examined through PET and magnetic resonance imaging (MRI) with this new technique and the data is combined with the appropriate pharmacokinetic compartmental analyses, the technique provides a critical tool for use in the analysis of brain function and its underlying neural network.

A secondary goal of extending the analysis using more optimal statistical reconstruction techniques for PET data, such as Bayesian MAP, is also accomplished. The image data reconstructed using statistical reconstruction routines more optimally model the physics of the imaging process. Parametric images of experimental data are generated using the DIRECT algorithm. Results are compared to results from standard compartmental model analyses. Good agreement with standard compartmental model fits is obtained, demonstrating the power of the method.

Thesis Supervisor: Anna-Liisa Brownell

Title: Associate Professor of Radiology, Harvard Medical School

## **Acknowledgements**

First and foremost, I would like to express my deepest gratitude to Dr. Anna-Liisa Brownell, my thesis advisor, for her invaluable guidance and support throughout this work. I have been fortunate to have such a wonderful mentor and role model in this area of scientific study. I would also like to thank Professor Derek Rowell, my thesis reader, for his involvement and guidance throughout this work. Finally, I would like to thank all who have worked by my side and extended their knowledge, kindness, and assistance: Dr. Iris Chen, Dr. Meixiang Yu, Chris Owen, Bob Powers, Dr. Tuan Cao-Huu, Jack MacDowell, David Kaufman, and Charles Burnham.

## Table of Contents

<b>Abstract</b>	<b>2</b>
<b>Acknowledgements</b>	<b>3</b>
<b>Table of Contents</b>	<b>4</b>
<b>List of Figures</b>	<b>6</b>
<b>List of Tables</b>	<b>7</b>
<b>1. Introduction</b>	<b>8</b>
1.1 Background	8
1.2 Objectives	13
<b>2. A Primate Model for Parkinson's Disease</b>	<b>15</b>
2.1 Animal Models for the Study of Parkinson's Disease	15
2.2 MPTP Treatment Regimen	17
<b>3. PET Imaging and PET Imaging System</b>	<b>18</b>
3.1 PET Imaging	18
3.2 Radiopharmaceutical Production	20
3.3 Imaging System	20
<b>4. Image Reconstruction, Correction and Analysis</b>	<b>24</b>
4.1 Image Reconstruction and Analysis	24
4.2 Image Correction	25
4.3 Convolution Backprojection	28
4.3.1 Radon Transform and Inverse Radon Transform	28
4.4 Bayesian MAP Reconstruction	31
4.5 Volumetric Fusion of PET with MRI	35
4.6 Region of Interest (ROI) Analysis	37
<b>5. Tracer Kinetic Modeling</b>	<b>38</b>
5.1 Compartmental Modeling	38
5.2 Parametric Imaging	40
5.2.1 Introduction	40
5.2.2 Parametric Image Model	42
5.2.3 The DIRECT Algorithm	45
<b>6. Research Design</b>	<b>51</b>
6.1 Experimental Work	51
6.2 Conventional Region of Interest (ROI) Analysis	52
6.2.1 Image Correction and Reconstruction	52
6.2.2 Time Activity Curves, Analysis and Results	54
6.3 Volumetric Region of Interest Analysis	59

6.3.1 Registration of PET and MRI Data	59
6.3.2 Time Activity Curves, Analysis and Results	63
6.4 Bayesian MAP Reconstruction	69
6.4.1 Registration of PET and MRI Data	71
6.4.2 Time Activity Curves, Analysis and Results	73
6.5 Parametric Image Analysis	76
6.5.1 Algorithm	76
6.5.2 Results	77
<b>7. Conclusions and Future Work</b>	<b>83</b>
7.1 Conclusions	83
7.2 Future Work	84
<b>References</b>	<b>86</b>

## List of Figures

<b>Figure 1.</b>	PET study of $^{11}\text{C}$ -CFT before and after MPTP	10
<b>Figure 2.</b>	PET study of $^{11}\text{C}$ -raclopride before and after MPTP	11
<b>Figure 3.</b>	Volume rendered fusion of PET $^{11}\text{C}$ -raclopride data with MRI data post MPTP	12
<b>Figure 4.</b>	PET study of $^{11}\text{C}$ -CFT and $^{11}\text{C}$ -raclopride binding before and after MPTP neurotoxicity	16
<b>Figure 5.</b>	PCR-I, a high resolution PET camera	21
<b>Figure 6.</b>	Primate head holder used for imaging studies.	22
<b>Figure 7.</b>	PET studies of $^{11}\text{C}$ -raclopride before MPTP and after MPTP	55
<b>Figure 8.</b>	PET studies of $^{11}\text{C}$ -CFT before MPTP and after MPTP	55
<b>Figure 9.</b>	PET studies of $^{11}\text{C}$ -raclopride before MPTP and after MPTP	56
<b>Figure 10.</b>	PET studies of $^{11}\text{C}$ -CFT before MPTP and after MPTP	56
<b>Figure 11.</b>	PET studies of $^{11}\text{C}$ -raclopride before MPTP and after MPTP	57
<b>Figure 12.</b>	PET studies of $^{11}\text{C}$ -CFT before MPTP and after MPTP	57
<b>Figure 13.</b>	T2 weighted MR images fused with PET images showing dopamine transporter binding ( $^{11}\text{C}$ -CFT) and dopamine D <sub>2</sub> receptor binding ( $^{11}\text{C}$ -raclopride) before MPTP	61
<b>Figure 14.</b>	PET study with $^{11}\text{C}$ -raclopride of dopamine D <sub>2</sub> receptors. PET images are fused with volume rendered MR images	62
<b>Figure 15.</b>	Regions of interest outlined on an MR image for application to its corresponding transformed PET image	63
<b>Figure 16.</b>	PET studies of $^{11}\text{C}$ -raclopride before and after MPTP	64
<b>Figure 17.</b>	PET studies of $^{11}\text{C}$ -CFT before and after MPTP	65
<b>Figure 18.</b>	PET studies of $^{11}\text{C}$ -raclopride before and after MPTP	65
<b>Figure 19.</b>	PET studies of $^{11}\text{C}$ -CFT before and after MPTP	66
<b>Figure 20.</b>	PET studies of $^{11}\text{C}$ -raclopride before and after MPTP	66
<b>Figure 21.</b>	PET studies of $^{11}\text{C}$ -CFT before and after MPTP	67
<b>Figure 22.</b>	PET studies using $^{11}\text{C}$ -raclopride and $^{11}\text{C}$ -CFT in the same primate before MPTP. PET images are reconstructed using Bayesian MAP with iterative coordinate descent.	72
<b>Figure 23.</b>	PET study of dopamine D <sub>2</sub> receptors using $^{11}\text{C}$ -raclopride. PET images are reconstructed using Bayesian MAP ICD and fused with volume rendered MR images.	72
<b>Figure 24.</b>	PET studies of $^{11}\text{C}$ -raclopride before and after MPTP	74
<b>Figure 25.</b>	PET studies of $^{11}\text{C}$ -CFT before and after MPTP	75
<b>Figure 26.</b>	Parametric images of M281 $^{11}\text{C}$ -CFT pre MPTP	78
<b>Figure 27.</b>	Parametric images of M458 $^{11}\text{C}$ -CFT pre MPTP	78
<b>Figure 28.</b>	Parametric images of M281 $^{11}\text{C}$ -raclopride pre MPTP treatment	79
<b>Figure 29.</b>	Parametric images of M458 $^{11}\text{C}$ -raclopride, post MPTP	79
<b>Figure 30.</b>	Parametric images of M458 $^{11}\text{C}$ -raclopride pre MPTP	80
<b>Figure 31.</b>	Parametric images of M463 $^{11}\text{C}$ -raclopride post MPTP	80
<b>Figure 32.</b>	Parametric images of M458 $^{11}\text{C}$ -raclopride	81
<b>Figure 33.</b>	Parametric images of M463 $^{11}\text{C}$ -raclopride post MPTP	81

## List of Tables

<b>Table 1.</b>	PC programs for image correction and reconstruction	<b>52</b>
<b>Table 2.</b>	Linux programs for correction of reconstructed data	<b>53</b>
<b>Table 3.</b>	Binding ratios from 2D ROI analysis of $^{11}\text{C}$ -raclopride	<b>58</b>
<b>Table 4.</b>	Binding ratios from 2D ROI analysis of $^{11}\text{C}$ -CFT	<b>58</b>
<b>Table 5.</b>	Binding potential values ( $k_3/k_4$ ) obtained from tracer kinetic model fits of $^{11}\text{C}$ -raclopride ROI data	<b>59</b>
<b>Table 6.</b>	Binding ratios from 3D ROI analysis of $^{11}\text{C}$ -raclopride	<b>67</b>
<b>Table 7.</b>	Binding ratios from 3D ROI analysis of $^{11}\text{C}$ -CFT	<b>68</b>
<b>Table 8.</b>	Binding potential values ( $k_3/k_4$ ) obtained from tracer kinetic model fits of $^{11}\text{C}$ -raclopride ROI data	<b>68</b>
<b>Table 9.</b>	Binding ratios from 3D ROI analysis of $^{11}\text{C}$ -raclopride data obtained through Bayesian MAP reconstruction	<b>75</b>
<b>Table 10.</b>	Binding ratios from 3D ROI analysis of $^{11}\text{C}$ -CFT data obtained through Bayesian MAP reconstruction	<b>76</b>
<b>Table 11.</b>	Binding potential values ( $k_3/k_4$ ) obtained from tracer kinetic model fits of $^{11}\text{C}$ -raclopride ROI data	<b>76</b>
<b>Table 12.</b>	Binding potential values ( $k_3/k_4$ ) obtained from parametric images	<b>82</b>

# Chapter 1

## Introduction

### 1.1 Background

Neurological disorders such as Parkinson's disease, Huntington's disease, and various forms of dystonia are thought to involve the deterioration of the central dopaminergic system [1]. Specifically, the most prominent pathological change in idiopathic Parkinson's disease is a degeneration of the nigrostriatal dopaminergic pathway. This degeneration is characterized by severe cell loss in the basal ganglia, which includes the substantia nigra, globus pallidus, putamen, caudate, nucleus accumbens and subthalamic nucleus, and leads to a substantial decrease in dopamine synaptic density and striatal dopaminergic concentrations. Striatal loss of dopamine results in the typical signs of Parkinson's disease, including akinesia, bradykinesia, rigidity, and resting tremor [1]. Other diseases, such as tardive dyskinesia and Tourette's syndrome, are also thought to involve abnormalities of the central dopaminergic system [1]. Analysis of dopaminergic receptors in the brain in vivo using positron emission tomography (PET) may be used to further understand the alterations in the dopamine system that either contribute to the pathophysiology of these conditions or play a major role in pharmacotherapy.

Nuclear medicine imaging using positron emission tomography has proven invaluable for obtaining physiological information and evaluating the extent of disease or therapeutic recovery in many diseases and disorders, including epilepsy, stroke, Parkinson's disease, Huntington's disease, and cancer [2]. The imaging technique

provides quantitative functional information by detecting the transport of a radiolabeled ligand through a tissue or organ. Furthermore, the technique also provides anatomical information based on the spatial distribution of the radioactive ligand. Using a variety of radiopharmaceuticals, it is possible to explore 1) regional blood flow, 2) glucose, oxygen, peptide and fatty acid metabolism, 3) pH distribution levels and 4) receptor binding as well as drug concentration and mechanisms in normal and diseased stages [2]. Positron emission tomography has provided the most information to date concerning the pathophysiology of stroke [2]. Positron emission tomography can be used to evaluate cerebral hemodynamics, glucose metabolism and oxidative metabolism in acute ischemic stroke in order to predict survival of the ischemic tissue and development and growth of the infarct. Positron emission tomography can also be used to further elucidate the pathophysiological mechanisms occurring in cancerous growths, and the imaging technique remains the most sensitive for localizing seizure foci in epilepsy [2].

In neurological disorders of the basal ganglia such as Parkinson's disease and Huntington disease, examination of the living brain by high-resolution positron emission tomography (PET), combined with the appropriate pharmacokinetic and physiological analyses, can provide valuable quantitative information of altered brain function. PET can also provide valuable quantitative information for the therapeutic evaluation of the treatment of Parkinson's disease through transplantation of fetal dopaminergic cells in selected areas of the brain [3]. The images obtained through tomographic reconstruction methods reflect functional information based on the spatial distribution of injected radiopharmaceuticals. The injected radioligands, depending on their design, can label either dopamine transporter or dopamine receptor binding sites located in specific

anatomical areas of the brain. Figure 1 shows results of dopamine transporter binding using carbon-11-labeled 2β-carbomethoxy-3β-(4-fluorophenyl) tropane (<sup>11</sup>C-CFT) in a 1-methyl-4-phenyl-1,2,3,6-tetrahydropyridine (MPTP) induced primate model of Parkinson's disease. MPTP is an injected neurotoxin that causes both oxidative stress and degeneration in the dopaminergic system and produces Parkinson's disease-like symptoms. Figure 2 shows results of dopamine D<sub>2</sub> receptor binding using <sup>11</sup>C-raclopride in an MPTP induced primate model of Parkinson's disease.

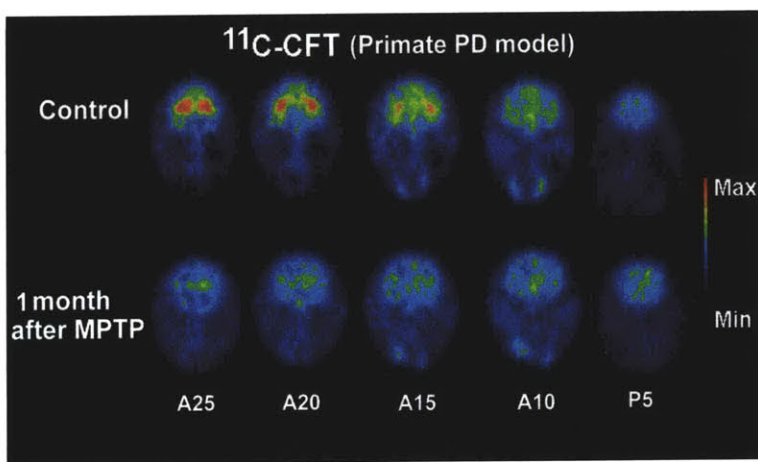


Figure 1. PET study of dopamine transporters (<sup>11</sup>C-CFT) before and after MPTP neurotoxicity. The five coronal slices at different brain levels (A25,A20,A15,A10, and P5) show the distribution of the <sup>11</sup>C-CFT accumulation 40-45 minutes post injection of the radioligand.

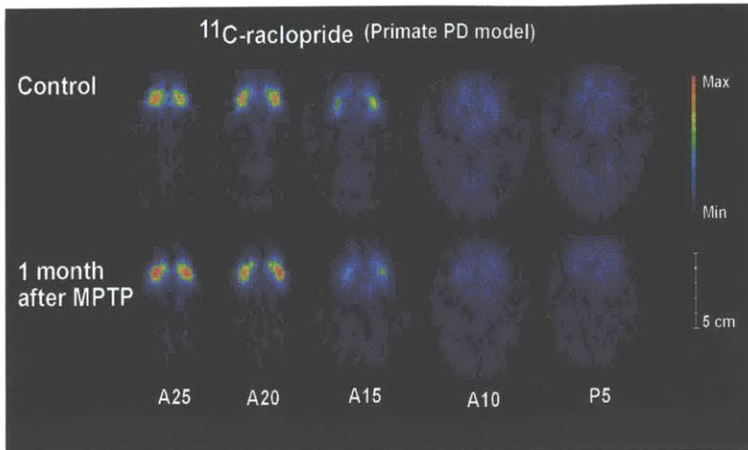


Figure 2. PET study of dopamine D2 receptor ( $^{11}\text{C}$ -raclopride) binding before and after MPTP neurotoxicity. Five coronal slices at the same brain levels as Figure 1 show the distribution of  $^{11}\text{C}$ -raclopride accumulation 40-45 minutes after injection of the radioligand.

Administered radiopharmaceuticals can also indicate cerebral glucose utilization or oxidative metabolism in specific anatomical areas of the brain. The functional information obtained through imaging studies can then be used to evaluate disease stages or therapeutic recovery. Research with positron emission tomography has added immeasurably to the understanding of flow, oxygen utilization, receptor density changes, and other metabolic changes accompanying disease and that change during brain stimulation and cognitive activation [2].

Along with advances in radiochemistry, which leads to the production of ligands that are capable of labeling specific binding sites within the brain, it is necessary to quantify functional data in these sites of the brain. PET images give poor anatomical structural information; yet they give highly sensitive functional information over small regions inside the brain, revealing underlying physiological processes. Magnetic resonance imaging (MRI), on the other hand, gives highly detailed structural information, showing different types of brain tissue as well as other soft tissue structures. Researchers are interested in determining which areas of the brain are involved in disease processes

and in functions such as movement or vision [4]. Therefore it is imperative to develop methods that allow one to reliably integrate the best information from each modality into a common reference system. This integration of information allows a greater level of accuracy in determining physiological parameters from tracer kinetic models and, in turn, for either elucidating the pathophysiological mechanisms from these models or for determining more accurate physiological models than can be obtained through the use of PET imaging alone. A result of this co-registration, or fusion, of multimodality information is shown in Figure 3. Here, a single slice from a PET study of  $^{11}\text{C}$ -raclopride  $\text{D}_2$  receptor binding in an MPTP induced primate model of Parkinson's disease is shown fused with its corresponding MRI data. Binding in the caudate and putamen areas is shown both functionally and anatomically.

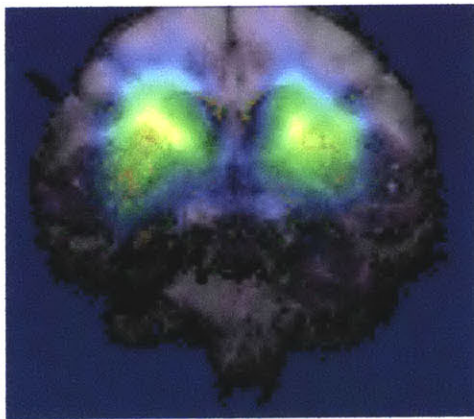


Figure 3. Volume rendered fusion (co-registration) of PET  $^{11}\text{C}$ -raclopride data with its corresponding MRI data post MPTP.

The research in this project focuses on quantifying the neuropathological and neurochemical alterations using both positron emission tomography and magnetic resonance imaging in an MPTP induced primate model of Parkinson's disease and using

experimental algorithms that have not been used to date for analyzing the physiological information obtained.

## **1.2 Objectives**

The primary objective of this work is to establish a volumetric process for the quantitative analysis of receptor function in a primate model of Parkinson's disease. The goal of this project is to determine if this analysis more accurately quantifies the neuropathological and neurochemical alterations observed in Parkinson's disease. A further goal is to gain a greater understanding of the disease.

Fusion of PET and magnetic resonance images provides the necessary step for combining the functional information obtained from PET with the anatomical information obtained from MRI. The benefit of having fused images is that it enables the visualization of functional PET data by superimposing it on a high-resolution anatomical MR image and therefore improves localization of radioligand-receptor binding and metabolic activity in the brain. Rendering of functional PET and anatomical MR images provides a three-dimensional visualization of information and further improves localization of radioligand-receptor binding and metabolic activity in the brain. Examination of the living brain through PET and MRI with this new technique, combined with the appropriate pharmacokinetic compartmental analyses, will provide a further tool for use in the analysis of brain function.

The research finally extends the analysis to constructing parametric images for determining receptor function. The algorithm used aims to construct parametric images directly from counts of radioactivity by combining the models for image reconstruction

with compartmental tracer-kinetic models. The direct process of constructing parametric images from reconstructed images using compartmental tracer-kinetic models forms in itself a difficult optimization problem that must in turn be explored in depth. The aim is to apply tracer kinetic models to both Bayesian maximum-a-posteriori reconstruction routines and convolution backprojection routines. Results are then compared to results originating from standard compartmental analyses.

## **Chapter 2**

### **A Primate Model for Parkinson's Disease**

#### **2.1 Animal Models for the Study of Parkinson's Disease**

Animal models have become invaluable towards understanding the neurochemical and pathophysiological changes characterizing these particular movement disorders. Animal models of movement disorders such as Parkinson's disease and Huntington's disease have been produced in primates, rats, and mice. Non-human primate models, in particular, have become invaluable since the primate brain has well-defined anatomical similarities to the human brain; and it has been possible to induce many human-like neural disorders in the primate brain for study of disease and therapeutic evaluation. Behavioral models of Parkinson's disease in cynomolgus monkeys (macaques) can be produced by either acute or chronic administration of the mitochondrial complex 1 inhibitor 1-methyl-4-phenyl-1,2,3,6-tetrahydropyridine (MPTP). Acute intravenous or intra-carotid injection of MPTP over 5 to 10 days induces a substantial dopaminergic depletion resulting in a severe akineto-rigid Parkinson's disease syndrome within weeks after administration of the neurotoxin [3]. Chronic MPTP treatment over longer periods of time (up to 19 months) more accurately produces the behavioral signs of idiopathic Parkinson's disease by inducing a selective loss of nigrostriatal dopamine neurons and creating oxidative stress. Repeated administration of the neurotoxin increases the selectivity for specific subpopulations of dopaminergic neurons; and the behavioral signs that can be correlated with this selective loss of nigrostriatal dopamine neurons develop gradually without the spontaneous recovery reported in some acute MPTP models [3].

The primate model produced by chronic administration of MPTP therefore represents the stable parkinsonian syndrome necessary for the exploration of long-term functional changes and experimental therapies [3].

Examination of the living brain over time using positron emission tomography in a primate that has undergone chronic MPTP treatment shows dopamine transporter loss with injection of the radiopharmaceutical,  $^{11}\text{C}$ -CFT, and  $\text{D}_2$  receptor supersensitivity with injection of the radiopharmaceutical,  $^{11}\text{C}$ -raclopride, and reveals the neuropathologically severe depletion of dopamine neurons and associated loss of axons and terminals characteristic of Parkinson's disease. Figure 4 shows results of dopamine transporter binding using  $^{11}\text{C}$ -CFT and dopamine  $\text{D}_2$  receptor binding using  $^{11}\text{C}$ -raclopride in an MPTP induced primate model of Parkinson's disease.

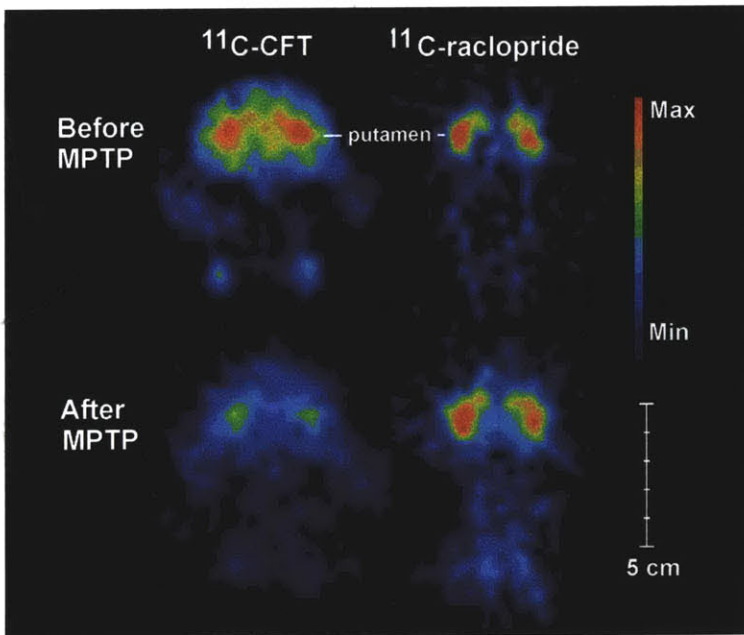


Figure 4. PET study of dopamine transporter ( $^{11}\text{C}$ -CFT) and dopamine  $\text{D}_2$  receptor ( $^{11}\text{C}$ -raclopride) binding before and after MPTP neurotoxicity.

Decreased binding of  $^{11}\text{C}$ -CFT in the striatum shows dopamine transporter loss, and the slightly increased binding of  $^{11}\text{C}$ -raclopride shows increased dopamine receptor

sensitivity in the striatum. Further analysis shows chronic MPTP treatment in primates models well the disease process observed clinically with PET in humans with Parkinson's disease.

## **2.2 MPTP treatment regimen**

More specifically, MPTP administration can be carried out using the following treatment regimens in non-human primates: repeated low doses (0.3-0.5 mg/kg bi-weekly) of MPTP intravenously over a 4-8 month period (chronic model) or repeated high doses (0.7 mg/kg daily) of MPTP over 1-5 days (acute model). These treatment regimens differ in many aspects. Acute MPTP treatment in non-human primates does not produce an uneven pattern of striatal dopamine loss described in the chronic MPTP model, with relative sparing of dopamine levels in the caudate nucleus compared to the putamen [5]. Furthermore, acute administration does not reproduce the chronic and slow degeneration of dopamine neurons that occurs in the chronic model; and spontaneous recovery of motor symptoms may occur with the acute model. For the primate studies used in this research, the following protocol was used: Five male monkeys (*Macaca fascicularis*) were injected with 0.5 mg/kg of MPTP biweekly until behavioral signs of Parkinson's disease appeared.

## Chapter 3

### PET Imaging and PET Imaging System

#### 3.1 PET Imaging

PET imaging begins with the injection, swallowing or inhalation of a metabolically active tracer carrying a positron-emitting isotope. The isotope accumulates in an area of the body for which the molecule has an affinity and resides there in concentrations that indicate levels of metabolic activity such as blood flow or the distribution of neuroreceptors. Different radiochemicals are needed to map different measures of metabolic activity. The radioactive nuclei then decay by positron emission. Each ejected positron combines with an electron almost instantaneously and undergoes the process of annihilation. The energy associated with the masses of the positron and electron is divided equally between two emitted photons, each with an energy of 511 keV, that travel outward in opposite directions from each other at a 180-degree angle. The high-energy gamma rays emerging from the body in opposite directions follow a Poisson distribution and are detected as a coincidence event by an array of detectors surrounding the patient. Each recorded coincidence event is related to a line of response (LOR), a line along which the annihilation took place. The area overlapped and enclosed by the LORs is the field of view (FOV). The angles and the positions of the LORs are saved as 2D tables known as sinograms. Each row of the sinogram corresponds to a projection profile at certain angle, and the bins of the row correspond to the detector pairs in that direction. After the data acquisition interval, or scan time, each sinogram

bin contains the number of detected events (counts) for its LOR. When one hundred thousand or more annihilation events are detected, depending on the requirements of the imaging device, an image is created using tomographic reconstruction procedures from the recorded projection data in the same manner as computed tomography. The reconstructed image is a temporal average of the spatial tracer distribution on the transaxial image plane over the data acquisition period. Quantitative accuracy is then achieved by eliminating the effect of body attenuation and scatter. Once corrected, the images obtained can then be analyzed through irreversible and reversible binding models, tissue ratios, equilibrium analyses, linear compartmental models applied to tracer doses to assess binding potential, and nonlinear models applied to multiple injection data with varying specific activities or blocking agents for quantitation.

The particular radiopharmaceuticals used in the analysis of dopaminergic receptor function include carbon-11-labeled (S)-3,5-dichloro-2,6-dihydroxy-N-(1-ethyl-2-pyrrolidinyl)methylbenzamide hydrobromide ( $^{11}\text{C}$ -raclopride, a postsynaptic  $\text{D}_2$  receptor marker and reversible  $\text{D}_2$  antagonist) and the cocaine analogue carbon-11-labeled 2 $\beta$ -carbomethoxy-3 $\beta$ -(4-fluorophenyl) tropane ( $^{11}\text{C}$ -CFT).  $^{11}\text{C}$ -CFT is a dopamine transporter marker that visualizes dopamine re-uptake sites located on presynaptic dopamine terminals. The radiopharmaceutical used in the analysis of glucose metabolism is 2-fluoro-deoxy-D-glucose ( $^{18}\text{F}$ -FDG). The radiopharmaceuticals used in the analysis of oxidative metabolism are oxygen-15-labeled oxygen ( $^{15}\text{O}_2$ ) and oxygen-15-labeled carbon dioxide ( $\text{C}^{15}\text{O}_2$ ).

All radiopharmaceuticals and radioactive gases used in primate studies were produced by the cyclotron facility at the Massachusetts General Hospital.

### 3.2 Radiopharmaceutical production of $^{11}\text{C}$ -CFT and $^{11}\text{C}$ -raclopride

Synthesis of  $^{11}\text{C}$ -CFT (half-life, 20 minutes) involves direct  $^{11}\text{C}$ -methyl iodide methylation of 2 $\beta$ -carbomethoxy-3 $\beta$ -(4-fluorophenyl) tropane (WIN 35,428) [6].  $^{11}\text{C}$ -methyl iodide is produced in an automated system following proton bombardment of  $\text{N}_2$  containing 0.5%  $\text{O}_2$  to yield  $^{11}\text{CO}_2$ . The  $^{11}\text{CO}_2$  is trapped in 0.4 ml of LAH (0.25M) in THF, dried under a stream of  $\text{N}_2$  gas by heating at 120 degrees Celsius. The  $\text{AlLiO-}^{11}\text{CH}_3$  is treated with 0.8 ml of a 57% solution of hydroiodic acid. The  $^{11}\text{C}$ -methyl iodide produced is then transferred as a gas using  $\text{N}_2$  to the reaction vial. A 400  $\mu\text{g}$  aliquot of the N-demethylated precursor (norCFT) in 0.3 ml DMSO is reacted with  $^{11}\text{CH}_3$  at 110 degrees Celsius for 5 minutes. HPLC purification of  $^{11}\text{C}$ -CFT is performed on a Waters C 18 cartridge using a solvent system of 60% methanol and 40% pH 7.3 pH buffer ( 2.75 g  $\text{KH}_2\text{PO}_4$ , 2 ml TEA in 1000 ml water). After solvent evaporation, the activity is dissolved in 6 ml saline, and the solution is filtered through a 0.22  $\mu\text{m}$  Millipore filter. The specific activity of the final product ranges from 1000-2000 Ci/mmol.

Radiosynthesis of  $^{11}\text{C}$ -raclopride ((S)-3,5,dichloro-2,6-dihydroxy-N-(1-ethyl-2-pyrrolidinyl)methylbenzamide hydrobromide, half-life, 20 minutes) involves  $^{11}\text{C}$ -methyl iodide methylation of the precursor and separation of the product using a semiprep HPLC [7].

### 3.3 Imaging System

Positron emission tomography studies used for this thesis were conducted using PCR-I, an in-house built single ring PET scanning system equipped with 360 bismuth

germinate (BGO) detectors and a computer controlled imaging table [8]. Figure 5 shows a photograph of PCR-I. Figure 6 shows the primate head holder used for imaging studies. Each detector element in the camera is 2 cm high and 3 cm deep. The width varies from 4 mm at the front to 4.5 mm at the light guide, permitting the detectors to be assembled in a continuous cylinder. The detectors are viewed through a cylindrical light guide by 90 photomultiplier tubes, each 0.75 inches in diameter. The inner diameter of the cylindrical detector array is 46 cm. The diameter of the reconstructed region is 28 cm.

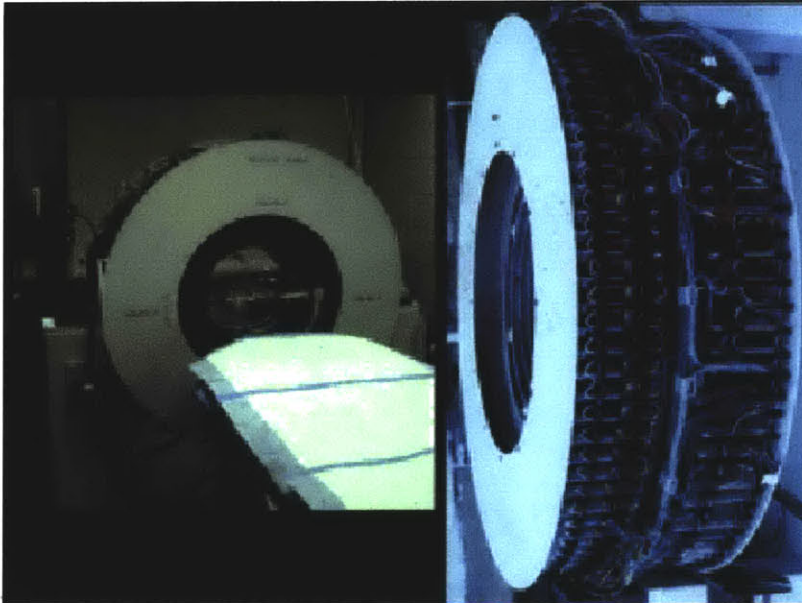


Figure 5. PCR-I, a high resolution PET camera built by Dr. Gordon Brownell, Charles Burnham, and David Kaufman at the Massachusetts General Hospital.

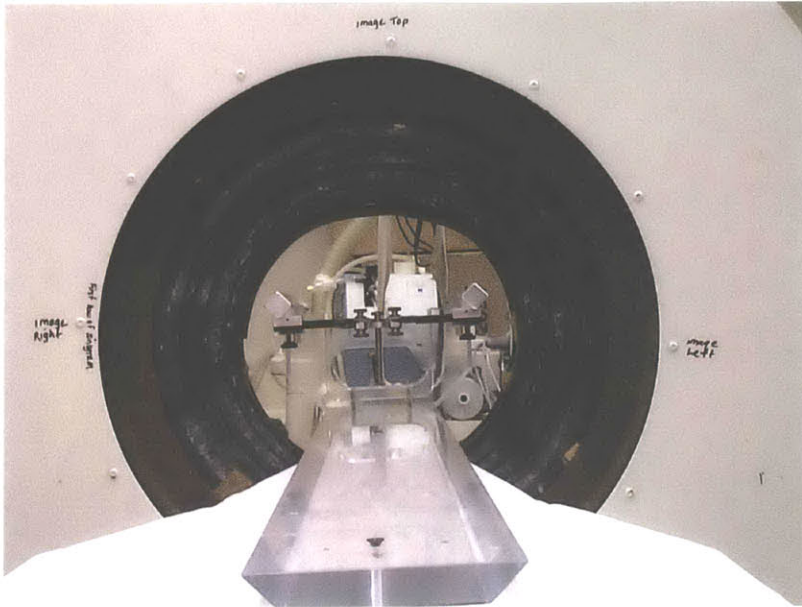


Figure 6. Primate head holder used for imaging studies.

The spatial resolution of PCR-I for a point source at the center is 4.5 mm (FWHM), with a sensitivity of 46,000 Hz/ $\mu$ Ci/cc (46,000 counts/sec for a source of 20 cm in diameter with a concentration of 1  $\mu$ Ci/cc). The overall efficiency of the detector is 64% of the theoretical maximum for a plane thickness corresponding to the 2 cm high detectors. The plane thickness of 5 mm used in the studies is obtained by limiting the effective height of the detectors with cylindrical collimators. The resolving time of PCR-I is 6 ns (FWHM), and the number of coincidence pairs of the device is 27,540.

Development of high-resolution PET systems is important for advancing the use of PET imaging for studying neurodegenerative disorders, particularly in smaller animal models using rats and mice. Though results will not be documented in this thesis, the author has also participated in the study and data analysis of rat and mouse disease models using an ultra-high resolution PET imaging device built by Charlie Burnham and

David Kaufman under the auspices of Jack Correia at the Massachusetts General Hospital.

Resolution in positron emission tomography is limited by a number of physical factors, including positron range, small angle deviation, and sampling frequency [8]. PCR-I, the first prototype tomograph employing the analog coding technique pioneered by Charles Burnham and known as the Burnham detector, was built in 1982. Analog coding permits the use of thick detectors needed by PET for high resolution, optimum positron sensing and use of light scintillation from BGO crystals, small system deadtime for high count rates and elimination of detector edge effects by employing the use of a matrix of crystals to control the spread of light from a scintillation event [8]. PCR-I achieves its adequate radial sampling through the use of the contiguous cylindrical detector elements implemented in its design [8]. Research continues in the production of other, smaller, ultra-high resolution tomographs using LGO crystals at the Massachusetts General Hospital.

PCR-I has demonstrated throughout its lifetime that high-resolution images can be obtained without interpolative motion [8]. Imaging sequences and gated images can be programmed without reference to motion, and allow volumetric reconstruction from “stacked” slices.

## **Chapter 4**

### **Image Reconstruction, Correction and Analysis**

#### **4.1 Image Reconstruction and Analysis**

There are broadly two classes of reconstruction algorithms used in positron emission tomography. The first class comprises deterministic methods based on the Radon transform, and includes such methods as filtered backprojection (FBP) and convolution backprojection (CBP). Here each recorded count is backprojected on to an appropriate subset of pixels using Fourier methods with the appropriate filter. The second class comprises statistical routines that aim to produce Bayesian or maximum likelihood estimates of parameters that describe the true mean rates of radioactivity in the pixels, and hence the radioisotope distribution, from the recorded counts at the detectors. With Bayesian reconstruction routines the choice of prior is essential; and estimation of the prior often includes the use of anatomical information retrieved from such imaging modalities as magnetic resonance imaging. The most common of the statistical routines that produce maximum likelihood estimates of these parameters includes the expectation maximization (EM) algorithm and the ordered subset expectation maximization (OSEM) algorithm.

Each of these reconstruction algorithms produces an image of the spatial distribution of radioactivity in the brain. The reconstructed image indirectly indicates rates of biochemical activity, which are monotonically related to the radioactivity levels present in the tissue. Tracer-kinetic models provide the usual mathematical link between measurements of radioactivity levels and estimates of physiological parameters. The

compartmental models represent biochemical processes. Each compartment represents one stage in a biochemical process. Differential equations describe how labeled compounds and their naturally occurring analogues flow between compartments. In first-order models constants govern the rates of flow between compartments. This same model represents local metabolism at every region of interest. The aim of compartmental modeling is to estimate particular model parameters, often involving a flow constant describing a local metabolic rate or neuroreceptor binding affinity. The type of compartmental model used depends on the radioligand involved in the study. For receptor studies a three-compartment model with four rate constants is commonly used. Compartment one represents tracer in blood plasma, compartment two represents unbound and nonspecifically bound tracer and compartment three represents tracer that is specifically bound to the receptors of interest. Most PET studies use nonlinear least squares regression for fitting these three-compartmental models.

## **4.2 Image Correction**

As mentioned previously, it is necessary to eliminate the effect of sensitivity, attenuation, and scatter in order to obtain quantitative accuracy for region of interest (ROI) analyses. Sensitivity to scattered coincidences, known as scatter, is greater in three-dimensional PET instruments with multiple septa than in two-dimensional single ring (one septum) PET instruments. It is a common practice to ignore the effects of scatter completely when single ring 2D PET instruments are used, since the contribution of scatter in the obtained signal is quite small. However, for 3D cameras the contribution of scatter in the obtained signal can become extremely large [9], and accurate scatter

correction methods, such as convolution-subtraction [10], Monte-Carlo modelling [11], direct measurement [12], Gaussian fit, model-based scatter correction, and multiple energy window methods [13], are required. Since PCR-I is a single ring device and the contribution of scattered coincidences is negligible, no scatter correction techniques are applied to the obtained experimental images.

The first correction applied to tomographic images obtained from PCR-I is the crystal sensitivity correction, which first computes the sensitivity of each crystal on the input uniform field sinogram collected from the camera, stores the calculated sensitivity matrix, and then applies this correction matrix to the input sinogram. The next correction applied to tomographic images obtained from PCR-I is attenuation correction.

Scatter from attenuation occurs when the emitted photons resulting from the original annihilation event interact with matter and scatter from their original, almost exact, 180-degree fly path. When this happens, true coincidence events do not occur; and not all annihilations are detected as tissue in the body attenuates the photon flux. The number of photons detected differs from the number of photons emitted, and the level of attenuation is a function of the tissue type traversed. Therefore, an attenuation correction method must be applied to positron emission tomography data in order to quantitatively determine the spatial emission source distribution.

Low energy photons, approximately 100 keV, interact with matter in three principal ways: Compton scattering, photoelectric effect, and pair production. Compton scattering is a photon-electron interaction where a photon collides with a free or nearly free electron, loses part of its energy to the electron, and then scatters in a new direction. In the photoelectric effect an atom absorbs a photon, and an electron is emitted from an

inner orbit of the atom. Pair production occurs when a photon with an energy greater than 1.022 MeV is completely absorbed by the nucleus of an atom, creating an electron-positron pair. The positron quickly annihilates with a nearby atomic electron, producing two 511 keV photons traveling in opposite direction. Since source photons from commonly used isotopes in PET are at energy levels considerably less than the 1.022 MeV required for pair production, only Compton scattering and the photoelectric effect are significant and the linear attenuation coefficient for each tissue type, measured by the number of photons removed from a collimated beam through absorption or scattering during traversal through the material, can be written as

$$\mu = \mu_{\text{Compton}} + \mu_{\text{photoelectric}} \quad (1)$$

The probability that both emitted photons from an annihilation event travel without scattering to the detectors is

$$P = P_1 P_2 = e^{-\int_{d_1} \mu(x) dx} e^{-\int_{d_2} \mu(x) dx} = e^{-\int_d \mu(x) dx}, \quad (2)$$

where  $\mu$  is the linear attenuation coefficient of the tissue type traversed to the detector pair, and  $d_1$  and  $d_2$  are the sub-paths from the location of the annihilation to the detector pair, whose total length through the tissue is  $d=d_1+d_2$ . Since positron emission tomography operates on coincidence detection, the attenuation effect is independent of the position of annihilation along the line of response. The attenuation of the annihilation photons depends on the thickness of the body for a constant attenuation coefficient and is independent of the position between detectors.

For tissue with constant attenuation coefficient,  $\mu$ , the number of photons that travel a distance  $x$  in the material imaged without being attenuated is

$$N(x) = N_0 e^{-\mu x} \quad (3)$$

where  $N_0$  is the original number of photons. For an object comprised of materials of different attenuation coefficients, the number of photons that travel a distance  $x$  in the material imaged without being attenuated becomes

$$N(x) = N_0 e^{-\int_0^x \mu(x') dx'} \quad (4)$$

where  $N_0$  is the original number of photons.

Attenuation correction is performed in PCR-I by computational means. The brain and other imaged soft tissues of the body can be treated using positron emission tomography as regions where the attenuation coefficient is constant, since the attenuation coefficient varies little through the different tissue types that are imaged in the body at the energy level of 511 keV. The numerical correction applied assumes the experimental subject's contour is an ellipse and the attenuation of the imaged tissue is uniform. The attenuation correction factors are computed in matrix format by graphically projecting the outlined  $\mu$ -image and taking the exponential,  $e^{-\int_d \mu(x) dx}$ , which is then applied to the input sinogram.

The final consideration in image correction is the partial volume effect. According to Hoffman [14] the resolution of the imaging device used should be at least half of the object size in order to avoid the partial volume effect. Since PCR-I has a resolution of 4.5 mm FWHM, half the size of the cynomolgus caudate-putamen complex, the partial volume effect is greatly reduced; and no partial volume correction is applied.

### 4.3 Convolution Backprojection

The image reconstruction process computes a two-dimensional slice of the object emitting radiation from its measured projections. The measured projections are stored in a sinogram and input to the reconstruction routine after a series of computational corrections for crystal sensitivity and attenuation. Noise and the finite number of measured projections make the reconstructed image an approximation of the true object. The properties of the image depend on the choice of the reconstruction method. The main differences between reconstruction methods come from how the data and its acquisition are modeled. One of the most common reconstruction methods used in emission tomography for physiological studies is the convolution backprojection technique, which models the data that is acquired by the Radon transform.

#### 4.3.1 The Radon Transform and the Inverse Radon Transform

The Radon transform is given by the following equation [15]

$$p(s, \theta) = R\{f\} = \int_{-\infty}^{\infty} \int_{-\infty}^{\infty} f(x, y) \delta(x \cos \theta + y \sin \theta - s) dx dy, \quad (5)$$

where the data measured,  $p(s, \theta)$ , is considered to be a set of line integrals passing through the two dimensional object given by  $f(x, y)$  at angle  $\theta$  ( $0 \leq \theta < \pi$ ). Note  $\theta$  is the projection angle and  $s$  is the detector location. The image  $f(x, y)$  representing the intensity of the emitted radiation at  $(x, y)$  may be reconstructed from its projections using the inverse Radon transform. This is based on the Fourier slice theorem, which states that the one dimensional Fourier transform of the projection taken at an angle  $\theta$  equals the central radial slice at angle  $\theta$  of the two dimensional Fourier transform of the original object. The one-dimensional Fourier transform of  $p(s, \theta)$  with respect to  $s$  is given by

$$P(\omega, \theta) = \int_{-\infty-\infty}^{\infty} \int_{-\infty}^{\infty} f(x, y) e^{-2\pi i \omega (x \cos \theta + y \sin \theta)} dx dy = F(\omega \cos \theta, \omega \sin \theta) = F(u, v), \quad (6)$$

where  $F(u, v)$  gives the values of the two-dimensional Fourier transform of  $f(x, y)$  evaluated along the line ( $u = \omega \cos \theta, v = \omega \sin \theta$ ) across  $(u, v)$  space. The inverse two-dimensional Fourier transform of the above equation using the polar coordinates  $\omega$  and  $\theta$  in  $(u, v)$  space is given by

$$\begin{aligned} f(x, y) &= \int_{-\infty-\infty}^{\infty} \int_{-\infty}^{\infty} F(u, v) e^{2\pi i (xu + yv)} du dv = \int_0^{\pi} \int_{-\infty}^{\infty} P(\omega, \theta) |\omega| e^{2\pi i \omega (x \cos \theta + y \sin \theta)} d\omega d\theta \\ &= \int_0^{\pi} \hat{p}(x \cos \theta + y \sin \theta, \theta) d\theta = B\{\hat{p}(s, \theta)\}, \end{aligned} \quad (7)$$

where  $B\{\hat{p}(s, \theta)\}$  is the backprojection of  $\hat{p}$  over the image and  $\hat{p}$  is defined as

$$\hat{p}(s, \theta) = \int_{-\infty}^{\infty} P(\omega, \theta) |\omega| e^{2\pi i \omega s} d\omega$$

using the Fourier slice theorem. The multiplication by  $|\omega|$

serves as a filter for each projection profile in the frequency space and the filtered profile  $\hat{p}$  is summed along the ray paths in the image space.

The most common algorithms used to compute the inverse Radon transform are filtered backprojection and convolution backprojection. For the convolution backprojection algorithm the sinogram data is pre-filtered as a convolution in the spatial domain before taking the backprojection. The backprojection step over the image at a given angle requires interpolation onto a square grid and is the most time consuming part of the routine. Images reconstructed using convolution backprojection in this thesis utilize Hanning-weighted convolution backprojection with a cutoff value of 1.0. Ramp filters or Hanning filters with varying cutoff values have also been used for rat data or

other image reconstructions. However, it is important to note that since measured data in emission tomography is intrinsically noisy and the ramp filter amplifies high frequencies, the ramp filter tends only to be used for reconstructing images when very high counts per pixel are obtained in the imaging of small objects like the rodent brain.

#### **4.4 Bayesian MAP Reconstruction**

Models for statistically optimal reconstruction and restoration of image data have played a prominent role in advancing medical imaging science in the last decade. Bayesian models using Gibbs priors have formed the core of this development; however, the use of Bayesian methods for image reconstruction has been hindered by their computational expense and questions over the prior distribution employed. The reasons statistical methods for image reconstruction have captured interest are twofold: 1) statistical noise is always present in the acquired projection data due to the random nature of radioactive decay; and 2), since noise is a random variable, each set of projection measurements is different for each acquisition, even for the same object. When data is noisy, direct inversion methods such as FBP or CBP are sensitive to this measurement noise; and image artifacts result. The inverse problem using direct inversion methods thus becomes ill-posed, and the problem can be made well-posed through probabilistic methods of reconstruction. For Bayesian methods the data is reconstructed based on a prior distribution, a predefined assumption about the true nature of the image, which gives information about the image independent of the measured data. The image is reconstructed by maximizing the *a posteriori* probability distribution function using Baye's theorem and generates the most likely image given the observed data. This form

of image reconstruction is called Bayesian maximum *a posteriori* , or Bayesian MAP, reconstruction.

In the last several years a variety of Bayesian reconstruction algorithms have been proposed for maximum a posteriori (MAP) reconstruction of emission computed tomography data. Most of these MAP algorithms employ the indirect approach based on the expectation maximization (EM) algorithm for solving the optimization problem required for MAP estimation. However, while MAP estimation requires the solution of an optimization problem; instead of using the EM algorithm to solve the optimization problem, an approach based on direct optimization of the MAP criterion developed by Charles Bouman and Ken Sauer using greedy pixel-wise computations known as iterative coordinate descent (ICD) may be utilized [16]. Bouman and Sauer have shown that ICD iterations require approximately the same amount of computation per iteration as EM based approaches, but their method converges much more rapidly [16]. The ICD method can be easily applied to MAP estimation of both emission and transmission tomograms; and typical convex constraints, such as positivity, may be simply incorporated [16]. This convex constraint of positivity is particularly useful for the optimization routine used to generate parametric images in chapter 5.

The statistical model Bouman and Sauer [16] created for emission tomography uses exact Poisson counting statistics and can be presented as follows: Let  $x$  be the  $N$  dimensional vector of emission rates and  $Y$  be the  $M$  dimensional vector of Poisson distributed photon counts.  $x_j$  represents the emission rate from pixel (voxel)  $j$ ,  $y$  is the vector of photon counts for all  $M$  projections at different angles and displacements, and  $P$  is the tomographic projection matrix.  $P_{ij}$  is the probability that an emission from

pixel  $j$  is registered by the  $i^{\text{th}}$  detector and corresponds to the length of intersection between the pixel  $j$  and the  $i^{\text{th}}$  projection. Baye's theorem gives for the random vector  $Y$  the probability distribution function for a Poisson process

$$p_{y|x}(Y = y|x) = \prod_{i=1}^M \frac{\exp\{-P_{i*}x\} \{P_{i*}x\}^{y_i}}{y_i!}, \quad (8)$$

where the matrix  $P$  contains the probabilities  $P_{ij}$  and  $P_{i*}$  denotes the vector formed by its  $i^{\text{th}}$  row. The log-likelihood is given by

$$\log p_{y|x}(Y = y|x) = \sum_{i=1}^M (-P_{i*}x + y_i \log\{P_{i*}x\} - \log(y_i!)) \quad (9)$$

for emission, which can be written as

$$\log p_{y|x}(Y = y|x) = -\sum_{i=1}^M f_i(P_{i*}x), \quad (10)$$

where the  $f_i(\cdot)$  are convex and differentiable functions. The prior model selected for the algorithm is the Generalized Gaussian Markov Random Field (GGMRF), which has been shown to better preserve edge detection than many other potential functions which have been used as priors, with a density function

$$p_x(x) = \frac{1}{z} \exp\{-\gamma^q \sum_{\{j,k\} \in C} b_{j-k} |x_j - x_k|^q\}, \quad (11)$$

where  $C$  is the set of all neighboring pixel pairs,  $z$  is a normalization constant,  $b_{j-k}$  is the coefficient linking pixels  $j$  and  $k$ ,  $\gamma$  is a scale parameter, and  $1 \leq q \leq 2$  is a parameter which controls the smoothness of the reconstruction. The use of Markov random fields as priors has proven successful in a number of applications for image reconstruction and restoration [16]. The GGMRF is a spatially homogeneous Markov

random field with a non-quadratic penalty term that provides edge detection without explicitly modeling edges [16]. Smaller values of  $q$ , in general, lead to sharper edges in the reconstructed images. The prior information is made available in the form of constraints on the reconstructed solution. The set of all feasible reconstructions,  $\Omega$ , which also happens to be a set of positive reconstructions, is convex; and the following expression for the MAP reconstruction results:

$$\hat{x}_{MAP} = \arg \min_{x \in \Omega} \left[ \sum_{i=1}^M f_i(P_i \cdot x) + \gamma^q \sum_{\{j,k\} \in C} b_{j-k} |x_j - x_k|^q \right], \quad (12)$$

a combination of the results in (10) and (11). This result can also be written as

$$\hat{x}_{MAP} = \arg \max_{x \in \Omega} \left[ \log p_{y|x}(y|x) + \log p_x(x) \right], \quad (13)$$

where  $\log p_{y|x}(y|x)$  is the Poisson log likelihood function.

An iterative coordinate descent algorithm is used for efficient direct optimization of the expression in (12). The basic concept of the ICD algorithm is to solve the expression using the Newton-Raphson approach. For each pixel  $x_j$  the update of the  $j^{\text{th}}$  pixel is given by

$$x_j^{n+1} = \arg \min_{\lambda \geq 0} \left[ \sum_{i=0}^M \left[ P_{ij} \lambda - y_i \log(P_{ij}(\lambda - x_j^n) + P_i \cdot x^n) \right] + \gamma^q \sum_{k \in N_j} b_{j-k} |\lambda - x_k^n|^q \right], \quad (14)$$

where  $N_j$  is the set of pixels neighboring  $j$ ; and the equation is applied sequentially for each pixel for full update of the image. A quadratic approximation is applied to the Poisson log likelihood function, the exact form of the log likelihood of the prior distribution is retained, and the Newton Raphson algorithm is used to update each pixel value  $x_j$  as follows:

$$x_j^{n+1} = \arg \min_{\lambda \geq 0} \left[ \phi_1(\lambda - x_j^n) + \frac{\phi_2}{2}(\lambda - x_j^n)^2 + \gamma^q \sum_{k \in N_j} b_{j-k} |\lambda - x_k^n|^q \right], \quad (15)$$

where

$$\phi_1 = -\frac{\partial}{\partial x_j} \log_{y|x} p(y|x) = \sum_{i=1}^M P_{ij} \left(1 - \frac{y_i}{\tilde{p}_i^n}\right) \quad (16)$$

$$\phi_2 = -\frac{\partial^2}{\partial x_j^2} \log_{y|x} p(y|x) = \sum_{i=1}^M y_i \left(\frac{P_{ij}}{\tilde{p}_i^n}\right)^2 \quad (17)$$

$$0 = \phi_1 + \phi_2(\lambda - x_j^n) + q\gamma^q \sum_{k \in N_j} b_{j-k} |\lambda - x_k^n|^{q-1} \text{sign}(\lambda - x_k^n) \Big|_{\lambda=x_j^{n+1}} \quad (18)$$

$$\tilde{p}^{n+1} = P_{*j}(x_j^{n+1} - x_j^n) + \tilde{p}^n \quad (19)$$

and

$$\tilde{p}_i = P_{i*}x \quad (20)$$

A drawback of Bayesian reconstruction routines is that the reconstructions possess spatially varying resolution [17]. High activity regions are regularized more strongly, which can be suboptimal for lesion data or other regions where high binding occurs [17]. An advantage of Bayesian reconstruction routines is that its reconstructions provide lower bias for region of interest (ROI) analyses than convolution backprojection algorithms. Another advantage of Bayesian reconstruction routines is that the algorithm is less sensitive to noise, since priors are selected to regularize the solution and impose smoothness constraints that eliminate high frequency noise.

#### 4.5 Volumetric Fusion of PET with MRI

Multi-modal medical image registration (co-registration, or fusion) of PET images and magnetic resonance (MR) images is essential for combining the functional information obtained from PET with the anatomical information obtained from MR. Co-registration of medical images is also important for surgical applications, such as neurosurgical tumor removal. The benefit of having fused images is that it enables the visualization of functional PET data by superimposing it on a high-resolution anatomical MR image and therefore improves localization of radioligand-receptor binding and metabolic activity in the brain. Rendering of functional PET and anatomical MR images provides a three-dimensional visualization of information and further improves localization of radioligand-receptor binding and metabolic activity in the brain.

Many image registration methods have been developed for these purposes. These image registration methods are divided into two groups: surface based techniques, which encompass global, affine, rigid body registration methods based on spatial landmarks or surfaces, and voxel-value-based techniques, which are based on relationships between the voxel values of different imaging modalities where the cost function is evaluated with different algorithms. An example of a voxel-value-based technique is the maximization of mutual information algorithm, where registration is achieved by adjusting the relative position and orientation until the mutual information defined in terms of entropy between the images is maximized [19].

Each co-registration method has attached to it some intrinsic method of registration error, which may not always give a true representation of the distance between actual and estimated positions of targets within the cranial cavity [18]. Landmark or surface-based registration techniques tend to register with overall accuracies

in the range of 1-2 voxels, while mutual information and voxel-based techniques tend to register with subvoxel accuracies [18].

The multi-modal volume registration method selected for this work is the normalized mutual information (NMI) voxel match algorithm provided by ANALYZE (Mayo Clinic, Biomedical Imaging Resource, Rochester, MN). This method uses mutual information, extensive image/volume sub sampling and a novel grayscale binning technique to effect as very fast and accurate registration. The algorithm employs a mutual information measure of registration cost and is considered one of the most robust and accurate algorithms for multimodality registration available to date.

#### **4.6 Region of Interest (ROI) Analysis**

Accuracy of image reconstruction and image correction forms a primary basis for the analysis of all images produced by emission tomography. Region of interest analysis is based on determining the activity in a selected region of tissue averaged over the selected set of image pixels/voxels; and both noise and reconstruction artifacts degrade the reliability of ROI analysis by causing some local bias to the quantitative values of ROI pixels/voxels, since by its nature data acquisition in emission tomography is subject to a substantial amount of statistical noise arising from the nature of the radioactive decay of the injected radiopharmaceutical. The use of statistical reconstruction routines in actual physiological analysis, which has been dominated by the use of convolution backprojection methods, should provide data with lower bias and provide a new method for routine analysis as the computational speed of computers on the market increases.

## Chapter 5

### 5.1 Compartmental Modeling

Dynamic models of many processes in the biological and physical sciences that depend on local mass balance conditions give rise to systems of ordinary differential equations, many of them nonlinear, called compartmental systems [20]. Tracer kinetic models, compartmental systems, are defined in physiology to model receptor binding *in vivo* in the brain using positron emission tomography. In these tracer kinetic models the brain consists of a number of compartments corresponding to different states of a tracer. The compartments in the compartmental system reflect the fate of the tracer and represent a specific biochemical theory.

Several models exist for estimating the neuroreceptor binding parameters ( $B_{\max}$ , the maximum number of available specific binding sites of a receptor;  $K_D$ , the dissociation constant;  $k_{\text{on}}$ , the bimolecular association rate constant; and  $k_{\text{off}}$ , the dissociation rate). The choice of model used depends on the particular properties of the radioligand-receptor interaction. In reversible binding, the ligands dissociate from the receptor during the imaging period so that the maximum binding site density can be calculated from the equilibrium distribution [21]. In irreversible binding equilibrium is not achieved during the imaging period.

Kinetic behavior of  $^{11}\text{C}$ -CFT and  $^{11}\text{C}$ -raclopride is studied with a four parameter estimation of a three compartmental, two-tissue compartmental model. The first compartment is the plasma pool, the second is the exchangeable tracer pool including free and nonspecifically bound ligand in the brain, and the third compartment is a trapped tracer pool including bound ligand in the brain. The kinetic parameters  $k_3$  and  $k_4$

describe the binding to and dissociation from the receptors. The differential equations used to describe the compartmental system are as follows:

$$\frac{dC_2(t)}{dt} = k_1 C_1(t) - k_2 C_2(t) - k_3^{\wedge} C_2(t) + k_4 C_3(t) \quad (21)$$

$$\frac{dC_3(t)}{dt} = k_3^{\wedge} C_2(t) - k_4 C_3(t), \quad (22)$$

where the parameter  $k_3^{\wedge}$  is defined as

$$k_3^{\wedge} = k_{on} f_2 [B_{max} - C_3(t)]. \quad (23)$$

Here,  $f_2$  describes the free fraction of the ligand in extracellular space.

Three types of kinetic analysis are used for analyzing PET data: graphical methods, including Logan plots and Patlak plots; equilibrium methods; and dynamic methods using general nonlinear regression techniques to solve the optimization problem posed by the tracer kinetic model. The choice of method used for analysis again depends on the properties of the radioligand-receptor interaction.

For compartmental modeling results presented in this thesis, the transfer coefficients  $k_1 - k_4$  are mathematically resolved using a nonlinear least squares fit, Levenberg-Marquardt method. All numerical optimization of time-activity curves from region of interest data is performed with the SAAM II program (SAAM Institute, University of Washington, Seattle, WA). For stabilization of k values the fitting procedure is performed in two steps. Since the cerebellum has negligible specific receptor binding, fitting is done in the cerebellum using a two compartment, one tissue compartment model letting all k values float. The ratio  $\frac{k_1}{k_2}$  is calculated. This ratio is

fixed and used as a constraint in the optimization of the three compartmental, two tissue compartmental model. Regional binding potential is calculated as  $\frac{k_3}{k_4}$ .

## **5.2 Parametric Imaging**

### **5.2.1 Introduction**

Tomographic image data obtained from PCR-I is essentially two-dimensional; however, the image slices may be combined into a three dimensional image for analysis. The time sequence of these emission tomographic images forms a three-dimensional (when used as 2D alone) or four-dimensional (when combined volumetrically) image that is medically important since tracer concentration in tissue both reflects its physiological state and changes with time.

Parameter estimation from compartmental tracer-kinetic models has become increasingly important for evaluating the extent of disease or therapeutic recovery in both research and clinical settings. An interest has developed in recent years towards estimating these parameters directly from the images themselves. The generation of a parametric image requires the fitting of a tracer-kinetic model to time activity curve data from a dynamic image sequence on a pixel-by-pixel (or voxel-by-voxel) basis. The parametric image computed from the dynamic image sequence results in a quantitative image that depicts the values of a certain rate (for example, metabolic rate), depending on the physiological or biochemical model employed. Parametric imaging is particularly important because it allows for the quantification of small regions of interest without the partial volume effect.

The various numerical algorithms that are used for parametric imaging differ in their generality, computational speed and statistical performance [22]. Some of the numerical methods used for parametric imaging include weighted nonlinear regression, Patlak analysis, sigmoidal networks, and the basis function method [23]. Weighted nonlinear regression is iterative, time-consuming, and derived from approximations that introduce error; however, the method has been found to offer good statistical performance [22]. Patlak analysis is generally suitable only for linear compartmental models. Approaches using sigmoidal networks, an artificial feed-forward neural network approach to solving both nonlinear and linear compartmental models, have been applied with success, particularly with myocardial perfusion data [22]. The basis function method developed by Roger Gunn, however, has received the most attention to date as a result of its speed and statistical performance. The method generates parametric images of radioligand-receptor binding using the simplified reference region compartmental model described by Blomquist [24] and Cunningham [25] and does not require the use of arterial plasma data as an input function. The method instead relies on the use of cerebellar time activity curves as its input function. Parameter estimates from the model are obtained from a set of basis functions, which allow the incorporation of parameter bounds.

A new method for parametric imaging is presented in this thesis. This method relies on a novel application of the DIRECT algorithm developed by Jones, Perttunen, and Stuckman [26] and allows for the global optimization of the compartmental tracer-kinetic model.

### 5.2.2 Parametric Image Model

A description of the compartmental tracer-kinetic model employed in order to determine the receptor binding potential of injected radiopharmaceuticals is described in this section. At ( $t = 0$ ) the radiolabeled ligand is injected into the arterial blood stream, with an arterial blood plasma concentration  $C_B(t)$ . A fraction of this arterial blood concentration,  $y$ , is carried by normal blood flow to the brain. At the blood brain barrier the tracer diffuses out of the lumen into the extravascular space, with a “free” tracer concentration  $C_f(t)$ , and becomes bound with receptor or transporter sites (depending on the injected compound) and with a “bound” tracer concentration  $C_b(t)$ . In the case of binding the tracer can return to the “free” concentration pool after being released by the receptor. The rate constant governing this interaction is given by  $k_4$ . Furthermore, the tracer can also leave the voxel if not transported across the lumen, which is governed by the solubility coefficient  $\lambda$ . The transport within the voxel can be written according to this two-tissue compartmental tracer kinetic model as:

$$\frac{dC_f(t)}{dt} = y \frac{\dot{Q}}{V_p} C_B(t) - \lambda y \frac{\dot{Q}}{V_p} C_f(t) - k_3 C_f(t) + k_4 C_b(t) \quad (24)$$

$$\frac{dC_b(t)}{dt} = k_3 C_f(t) - k_4 C_b(t) \quad (25)$$

For simplicity,  $k_1$  and  $k_2$  are defined as:

$$k_1 = y \frac{\dot{Q}}{V_p}, \quad k_2 = \lambda \quad (26)$$

The concentration of radioactive tracer in the arterial blood,  $C_B(t)$ , provides the input function in the form of the double exponential

$$C_B(t) = A_1 \exp\left(-\frac{t}{\tau_1}\right) + A_2 \exp\left(-\frac{t}{\tau_2}\right). \quad (27)$$

In each voxel both free and bound tracer is indistinguishable from one another. Only the total tracer amount in the tissue can be measured by PET instrumentation

$$C_T(t) = C_f(t) + C_b(t).$$

The above set of first order differential equations can be solved simultaneously using Laplace transforms to give the total tracer concentration in each voxel as a function of time using the initial conditions  $C_f(0) = 0$  and  $C_b(0) = 0$  at  $t = 0$ . The following

solution results:

$$\begin{aligned} C_T(t) = & \frac{k_1 A_1}{\alpha_1 - \alpha_2} \left( \frac{\alpha_1 - (k_3 + k_4)}{\frac{1}{\tau_1} - \alpha_1} \right) \exp(-\alpha_1 t) (1 - \exp(\frac{1}{\tau_1} - \alpha_1)) \\ & + \frac{k_1 A_1}{\alpha_1 - \alpha_2} \left( \frac{(k_3 + k_4) - \alpha_2}{\frac{1}{\tau_1} - \alpha_2} \right) \exp(-\alpha_2 t) (1 - \exp(\frac{1}{\tau_1} - \alpha_2)) \\ & + \frac{k_1 A_2}{\alpha_1 - \alpha_2} \left( \frac{\alpha_1 - (k_3 + k_4)}{\frac{1}{\tau_2} - \alpha_1} \right) \exp(-\alpha_1 t) (1 - \exp(\frac{1}{\tau_2} - \alpha_1)) \\ & + \frac{k_1 A_2}{\alpha_1 - \alpha_2} \left( \frac{(k_3 + k_4) - \alpha_2}{\frac{1}{\tau_2} - \alpha_2} \right) \exp(-\alpha_2 t) (1 - \exp(\frac{1}{\tau_2} - \alpha_2)) \end{aligned} \quad (28)$$

, where

$$\alpha_1 = \frac{k_1 k_2 + k_3 + k_4}{2} + \left[ \left( \frac{k_1 k_2 + k_3 + k_4}{2} \right)^2 - k_1 k_2 k_4 \right]^{1/2} \quad (29)$$

$$\alpha_2 = \frac{k_1 k_2 + k_3 + k_4}{2} - \left[ \left( \frac{k_1 k_2 + k_3 + k_4}{2} \right)^2 - k_1 k_2 k_4 \right]^{1/2} \quad (30)$$

Image acquisition from positron emission tomography represents the integration of counts from a time  $t_1$  to  $t_2 = t_1 + \Delta t$ , taking into account the radioactive decay of the tracer, where  $\Delta t$  is the scan time per image frame. The number of counts per voxel  $\rho$  becomes

$$\rho = K_{cam} \int_{t_1}^{t_1 + \Delta t} V_p C_T(t) A_o \exp\left(-\frac{t}{\tau_d}\right) dt \quad (31)$$

where  $K_{cam}$  is the PET camera calibration factor relating the measure of count rate to the specific activity and  $A_o$  is the injected activity of the radiopharmaceutical. The counts originating from the blood have been neglected since  $V_p \gg V_{Bl}$  and  $C_B \approx 0$  when imaging begins. Integrated, the counts per voxel  $\rho$  obtained from the reconstructed images become

$$\begin{aligned} \rho = & \frac{K_{cam} V_p A_1 A_o k_1}{\alpha_1 - \alpha_2} \left( \frac{\alpha_1 - (k_3 + k_4)}{\frac{1}{\tau_1} - \alpha_1} \right) \left[ \tau_{e1} \exp\left(-\frac{t_1}{\tau_{e1}}\right) \exp\left(\frac{\Delta t}{\tau_{e1}} - 1\right) - \tau_{es1} \exp\left(-\frac{t_1}{\tau_{es1}}\right) \exp\left(\frac{\Delta t}{\tau_{es1}} - 1\right) \right] \\ & + \frac{K_{cam} V_p A_1 A_o k_1}{\alpha_1 - \alpha_2} \left( \frac{(k_3 + k_4) - \alpha_2}{\frac{1}{\tau_1} - \alpha_2} \right) \left[ \tau_{e1} \exp\left(-\frac{t_1}{\tau_{e1}}\right) \exp\left(\frac{\Delta t}{\tau_{e1}} - 1\right) - \tau_{es2} \exp\left(-\frac{t_1}{\tau_{es2}}\right) \exp\left(\frac{\Delta t}{\tau_{es2}} - 1\right) \right] \\ & + \frac{K_{cam} V_p A_2 A_o k_1}{\alpha_1 - \alpha_2} \left( \frac{\alpha_1 - (k_3 + k_4)}{\frac{1}{\tau_2} - \alpha_1} \right) \left[ \tau_{e2} \exp\left(-\frac{t_1}{\tau_{e2}}\right) \exp\left(\frac{\Delta t}{\tau_{e2}} - 1\right) - \tau_{es1} \exp\left(-\frac{t_1}{\tau_{es1}}\right) \exp\left(\frac{\Delta t}{\tau_{es1}} - 1\right) \right] \\ & + \frac{K_{cam} V_p A_2 A_o k_1}{\alpha_1 - \alpha_2} \left( \frac{(k_3 + k_4) - \alpha_2}{\frac{1}{\tau_2} - \alpha_2} \right) \left[ \tau_{e2} \exp\left(-\frac{t_1}{\tau_{e2}}\right) \exp\left(\frac{\Delta t}{\tau_{e2}} - 1\right) - \tau_{es2} \exp\left(-\frac{t_1}{\tau_{es2}}\right) \exp\left(\frac{\Delta t}{\tau_{es2}} - 1\right) \right] \end{aligned} \quad (32)$$

where

$$\tau_{e1} = \frac{\tau_1 \tau_d}{\tau_1 + \tau_d}, \tau_{es1} = \frac{\tau_d}{1 + \alpha_1 \tau_d}, \tau_{es2} = \frac{\tau_d}{1 + \alpha_2 \tau_d}, \tau_{e2} = \frac{\tau_2 \tau_d}{\tau_2 + \tau_d} \quad (33)$$

Knowing  $\rho$  on an image basis and the relevant constants, the expression may be fit to the acquired images using a global optimization routine on a voxel basis to yield images of  $k_1, k_2, k_3, k_4$  and finally

$$BP = \frac{B_{max}}{K_D} = \frac{k_3}{k_4} \quad (34)$$

### 5.2.3 The DIRECT algorithm

The n-dimensional DIRECT, short for dividing rectangles, a primary operation in the algorithm, algorithm for global optimization was developed by Jones, Perttunen, and Stuckman [26]. The form of the implemented method finds the global minimum of a multivariate function subject to simple bounds without the need to specify a Lipschitz constant and represents a modification to the standard Lipschitzian approach of Shubert's algorithm. The optimization routine performs better than n-bisection routines [27] and conducts simultaneous searches in all directions using all possible Lipschitz constants, weighting first at the global level, then conducting refinements at the local level once it finds and clusters its search near the basin of convergence of the optimum.

Jones, Perttunen, and Stuckman consider the problem of finding the global minimum of a function  $f(x)$  on a closed interval  $[l, u]$ . By definition, for Lipschitz continuous functions there exists a finite bound on the rate of change of the function called the Lipschitz constant, or  $\gamma$ , such that

$$|f(x) - f(x')| \leq \gamma \|x - x'\| \quad (35)$$

for all  $x, x' \in [l, u]$

For a hypothetical function defined on the interval  $[a, b]$  the idea of Lipschitz

optimization is to set  $x' = a$  and  $x' = b$  in (35) to obtain the following two inequalities

$$f(x) \geq f(a) - \gamma(x - a) \quad (36)$$

$$f(x) \geq f(b) + \gamma(x - b) \quad (37)$$

two lines with slope  $+\gamma$  and  $-\gamma$  from which a piecewise linear function  $\hat{f}$  may be constructed such that

$$\hat{f}(x) \leq f(x) \text{ for all } x \in [a, b] \quad (38)$$

and  $\hat{f}$  is given by the following

$$f(a) - \gamma(x - a), \quad x \in [a, x(a, b)] \quad (39)$$

$$f(b) + \gamma(x - b), \quad x \in [x(a, b), b] \quad (40)$$

where  $x(a, b)$  is

$$x(a, b) = \frac{[f(a) - f(b)]}{2\gamma} + \frac{(a + b)}{2} \quad (41)$$

and the minimum value of the function  $\hat{f}$  is given by

$$B(a, b) = \frac{[f(a) + f(b)]}{2} - \gamma(b - a) \quad (42)$$

These equations, (41) and (42), form the core of Shubert's algorithm [26].

The basic idea of the one-dimensional form of the DIRECT algorithm is to shift from sampling endpoints to sampling center points over "potentially optimal" intervals. The algorithm selects and samples within all potentially optimal intervals during an iteration. It divides the original interval into three intervals of equal length and evaluates the function at the midpoints of the three intervals. The algorithm then identifies the potentially optimal intervals and divides these intervals into thirds at the next iteration.

Using (35) again assume for an interval  $[a, b]$

$$|f(x) - f(x')| \leq \gamma \|x - x'\| \text{ for all } x, x' \in [a, b] \quad (43)$$

Let  $c = (a + b)/2$  and set  $x' = c$ . Then for all  $x \in [a, b]$

$$x \in [a, c]: f(c) + \gamma(x - c) \leq f(x) \leq f(c) - \gamma(x - c) \quad (44)$$

$$\text{and } x \in [c, b]: f(c) - \gamma(x - c) \leq f(x) \leq f(c) + \gamma(x - c) \quad (45)$$

with a lower bound  $f(c) - \gamma(b - a)/2$  for  $f$  in  $[a, b]$ .

The potentially optimal intervals are defined using different values of the Lipschitz constant as follows:

Suppose we have partitioned the interval  $[l, u]$  into intervals  $[a_i, b_i]$  with midpoints  $c_i$  for  $i = 1, \dots, m$ . Let  $\varepsilon > 0$  be a small positive constant and let  $f_{\min}$  be the current best

function value. Interval  $j$  is said to be potentially optimal if there exists some rate of

change constant  $\hat{K} > 0$  such that

$$f(c_j) - \hat{K}(b_j - a_j)/2 \leq f(c_i) - \hat{K}(b_i - a_i)/2 \text{ for all } i = 1, \dots, m \quad (46)$$

$$f(c_j) - \hat{K}(b_j - a_j)/2 \leq f_{\min} - \varepsilon |f_{\min}|. \quad (47)$$

Equation (46) expresses the decision to only choose intervals that promise the best

improvement in the function value if  $f$  is continuous with a rate of change constant  $\hat{K}$ .

Equation (47) ensures the possibility of a sufficient decrease in the interval to keep the

algorithm from being too local in its search. It has been found that  $\varepsilon$  values between

$10^{-3}$  to  $10^{-7}$  provide good results [28] for the algorithm. Furthermore, the potentially

optimal intervals are identified as follows:

Let  $\varepsilon > 0$  be a small positive constant and let  $f_{\min}$  be the current best function value. Let

$I$  be the set of all indices of all intervals  $d_i = (b_i - a_i)/2, j \in I$  given. Let

$I_1 = \{i \in I : d_i < d_j\}, I_2 = \{i \in I : d_i > d_j\}$  and  $I_3 = \{i \in I : d_i = d_j\}$  be given [28].

Interval  $j$  is potentially optimal if

$$f(c_j) \leq f(c_i)$$

for all  $i \in I_3$  and there exists a rate of change constant  $\hat{K} > 0$  such that

$$\max_{i \in I_1} \frac{f(c_j) - f(c_i)}{d_j - d_i} \leq \hat{K} \leq \min_{i \in I_2} \frac{f(c_i) - f(c_j)}{d_i - d_j}, \quad (48)$$

and

$$\varepsilon \leq \frac{f_{\min} - f(c_j)}{|f_{\min}|} + \frac{d_j}{|f_{\min}|} \min_{i \in I_2} \frac{f(c_i) - f(c_j)}{d_i - d_j}, \text{ if } f_{\min} \neq 0, \quad (49)$$

or

$$f(c_j) \leq d_j \min_{i \in I_2} \frac{f(c_i) - f(c_j)}{d_i - d_j}, \text{ if } f_{\min} = 0. \quad (50)$$

In the DIRECT algorithm the potentially optimal intervals are returned by the convex hull of a set of arbitrary points determined by a variation of the GRAMSHULL algorithm. [26]

The one-dimensional form of the DIRECT algorithm can be generalized to n-dimensions, scaling the search space with a lower bound of zero and an upper bound of one without loss of generality. The search space then becomes the n-dimensional unit hypercube. The center point of the hypercube is first evaluated. Then points are sampled at one-third the cube side length in each coordinate direction from the center point. Depending on the direction with the smallest function value, the hypercube is then subdivided into smaller rectangles, potentially optimal rectangles, with each sampled point becoming the center of its own n-dimensional rectangle or box. All boxes are identified by their center point  $c_i$  and their function value  $f(c_i)$  at that point [27]. The algorithm then iterates according to its subdivision of potentially optimal n-dimensional

boxes until termination or convergence. By using different values of the Lipschitz constant, a set of potentially optimal boxes is identified from the set of all boxes. The algorithm [27] is as follows:

1. Normalize the search space to the unit hypercube. Let  $c_1$  be the center point of the hypercube and evaluate  $f(c_1)$ .
2. Identify the set  $S$  of potentially optimal rectangles (those rectangles defining the bottom of the convex hull of a scatter plot of rectangle diameter versus  $f(c_i)$  for all rectangle centers  $c_i$ ).
3. For all boxes or rectangles  $j \in S$ :
  - 3a. Identify the set  $I$  of dimensions with the maximum side length. Let  $\delta$  equal one-third of this maximum side length.
  - 3b. Sample the function at the points  $c \pm \delta e_i$  for all  $i \in I$ , where  $c$  is the center of the rectangle and  $e_i$  is the  $i^{\text{th}}$  unit vector.
  - 3c. Divide the rectangle containing  $c$  into thirds along the dimensions in  $I$ , starting with the dimension with the lowest value of  $f(c \pm \delta e_i)$  and continuing to the dimension with the highest  $f(c \pm \delta e_i)$ .
4. Repeat steps 2 and 3 until the convergence or termination criterion is met.

The DIRECT algorithm has proven useful for optimizing nonlinear control systems and evaluating large-scale engineering designs; and it has proven itself well suited for optimization with the noisy function values typical of realistic simulations [27]. These results and the fact the algorithm allows for the specification of simple bounds for optimization make it attractive to apply to the problem of generating parametric images.

Image data generated by PET tends to be noisy; and even typical time activity curve fits tend not to be so straightforward when even using the standard optimization technique of nonlinear least squares regression, Levenberg-Marquardt method. The DIRECT algorithm allows for a unique approach for generating parametric images by treating the problem as a global optimization of the tracer-kinetic compartmental model on a voxel-by-voxel basis including plasma input instead of using generalized methods such as the basis function method. Furthermore, since the DIRECT algorithm has been shown to be computationally efficient in optimization with a standard set of test functions [26]; it is expected the algorithm will be relatively efficient for generating parametric image solutions.

## Chapter 6

### Research Design

#### 6.1 Experimental Work

Research is performed using actual experimental data from past and current primate studies. Imaging data for each raclopride or CFT study is collected in a 90 minute imaging session. Depending on ligands used, at least two imaging studies on the same animal are conducted in one day. The non-human primates used in the experiments include predominantly macaques (*Macaca fascicularis*), but studies have also included rhesus monkeys. The data used for this research are from five male monkeys (macaques) injected with 0.5 mg/kg MPTP weekly until Parkinson's disease-like symptoms appeared.

For imaging studies each animal is anesthetized with ketamine/xylazine (30/3 mg/kg) i.m. initial dose. Catheterization is then performed on the femoral artery and vein for collection of blood samples and injection of radiolabeled ligand, respectively. The animal is intubated and placed into imaging position, with the head adjusted into a specially designed stereotactic head holder with earbars at the origin. Interior orbital supports ensure that images are acquired on the pseudocoronal plane perpendicular to the orbito-metal line. This allows superposition and fusion of the data from MRI studies. Anesthesia is then maintained using halothane (1.5 % with 3 L oxygen flow rate). Injection of the radiolabeled ligand occurs afterward, with the start of imaging session beginning at mid-injection.

Dynamic imaging data for each study is collected 'stepwise' at seven coronal levels: A30 (30 mm anterior from the earbar), A25, A20, A15, A10, and P5 (5mm

posterior from the earbar). The initial acquisition time for each image is set to 15s; it is then increased to 30s per image, followed by 60s per image and finally either 60s or 90s per image. Twenty-one arterial blood samples of 0.3 ml are drawn to monitor the decrease of radioactivity, starting at a frequency of 15s and ending with a frequency of 10 minutes over the 90 minute imaging session. Calibration of each positron emission tomograph is done using results of a cylindrical plastic phantom (diameter 6 cm) and  $^{18}\text{F}$ -labeled water. Plasma data taken during each session is corrected for counting efficiency, calibration factor and measured metabolites; and percent activity of the injected dose and ligand concentration are calculated.

## 6.2 Conventional Region of Interest (ROI) Analysis

### 6.2.1 Image Correction and Reconstruction

Imaging data is corrected for uniformity, sensitivity, and attenuation using several programs written in C (denoted as \*.c) (see Table 1).

Table 1. Personal computer programs written in C that are used to both correct and reconstruct the raw sinograms collected during a PET scan.

PC Program	Function
Sen.c	Sets up sensitivity matrices for each sinogram
Sencor.c	Corrects raw image data (sinogram) for nonuniform crystal sensitivity
Elltrn.c	Creates transmission matrix for attenuation correction
Trncor.c	Takes a sinogram and transmission matrix and corrects for attenuation
Convbkpr.c	Reconstructs 2D imaging data using Hanning weighted convolution backprojection with a selected cutoff value or Ramp filtered convolution backprojection

The imaging data is then reconstructed and ported to a Linux workstation, where the images are corrected for decay, camera calibration, and collection time using scripts and another series of programs written in C and Matlab (Mathworks, Natick, MA), denoted as \*.c and \*.m, respectively. (see Table 2).

Table 2. Linux workstation programs written in C and Matlab for correcting reconstructed image data.

Linux Workstation Program	Function
Read_info.c	Reads image data, creates time data, and creates info files used for data conversion to bshort format
Ex_pet2.c	Corrects image data from first study for decay, calibration, and collection time and converts it to bshort format
Ex_pet.c	Converts image data directly to bshort format
Decay1.m (for multiple studies only)	Corrects last set of image data from first study for further decay during a subsequent study. Prepares the data to be subtracted from imaging data acquired during a later study
Decay2.m (for multiple studies only)	Corrects imaging data from a second study on the same animal for decay
Ex_pet3.c (for multiple studies only)	After subtracting imaging data acquired during the first study from imaging data acquired during a second study, this program then corrects the imaging data for camera calibration and collection time

After the image data is corrected, the images are repacked into 2D serial slices using repack.c and converted into ANALYZE/AVW image format. Regions of interest (including left and right caudate and putamen, frontal cortex and cerebellum) forming the conventional ROI analysis of each level of interest are outlined from anatomical representations on the screen in ANALYZE, and activity per unit volume, percent

activity of the injected dose and ligand concentration are calculated. The data obtained through ROI analysis is analyzed using a three compartmental model of receptor function and the SAAM II program. The plasma data obtained during each experiment provides the input functions used to complete the pharmacokinetic and physiological analyses. Final results from step one are then averaged for comparison with the results ultimately obtained from volumetric quantitative analysis.

### 6.2.2 Time Activity Curves, Analysis and Results

Time activity curves are generated from the conventional ROI analysis. Results from PET studies of  $^{11}\text{C}$ -raclopride and  $^{11}\text{C}$ -CFT in a MPTP induced primate model of Parkinson's disease are shown in Figures 7,8,9,10,11 and 12. The earlier dates are pre MPTP; later dates are post MPTP treatment. Binding ratios for  $^{11}\text{C}$ -CFT are determined as a ratio of graphically integrated activity concentrations (40-60 minutes) in the region of interest and cerebellum [Binding Ratio = ( $\int\text{ROI} / \int\text{cerebellum} - 1$ )]. Binding ratios for  $^{11}\text{C}$ -raclopride are determined as a ratio of graphically integrated activity concentrations (about the equilibrium point of 40-42 minutes) in the region of interest and cerebellum [Binding Ratio = ( $\int\text{ROI} / \int\text{cerebellum} - 1$ )]. The percent difference between the striatum and the cerebellum is then calculated. Results are shown in Tables 3 and 4.

Compartmental model fits of  $k_1 - k_4$  using SAAM II were performed, and resulting  $\frac{k_3}{k_4}$  values are shown in Table 5. Blood data is fitted to a biexponential function, which is then used as an input in fitting the time activity curve data to the set of differential equations of the compartmental model.

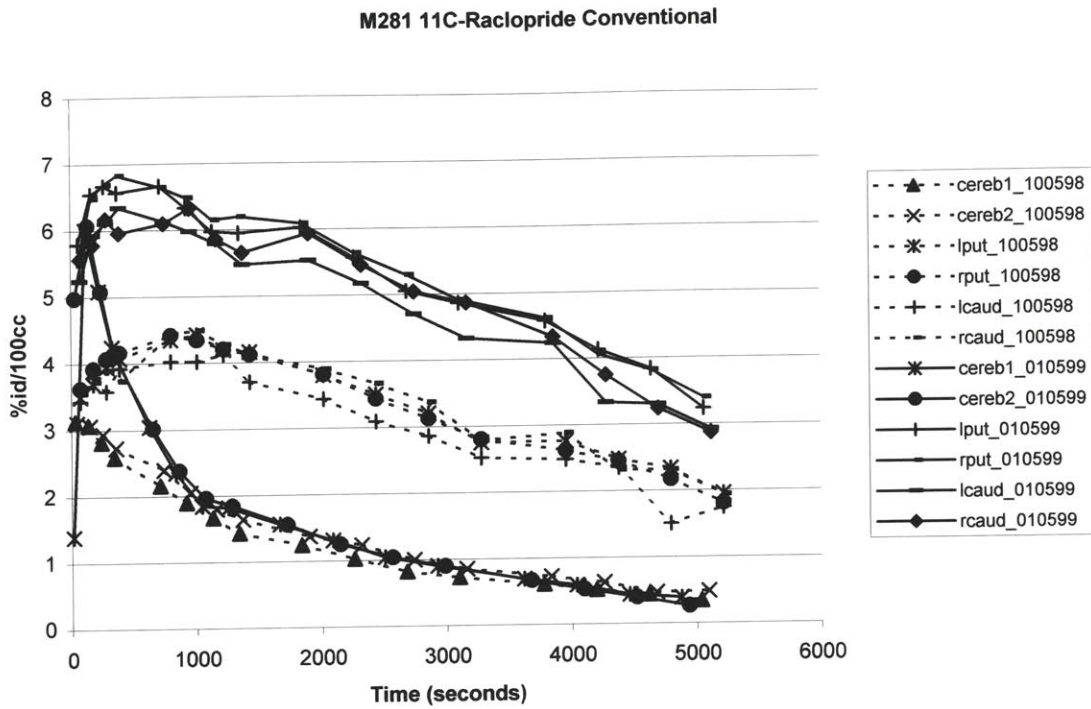


Figure 7. PET studies of  $^{11}\text{C}$ -raclopride in a nonhuman primate. 10/05/1998 – before MPTP. 01/05/1999 – after MPTP.

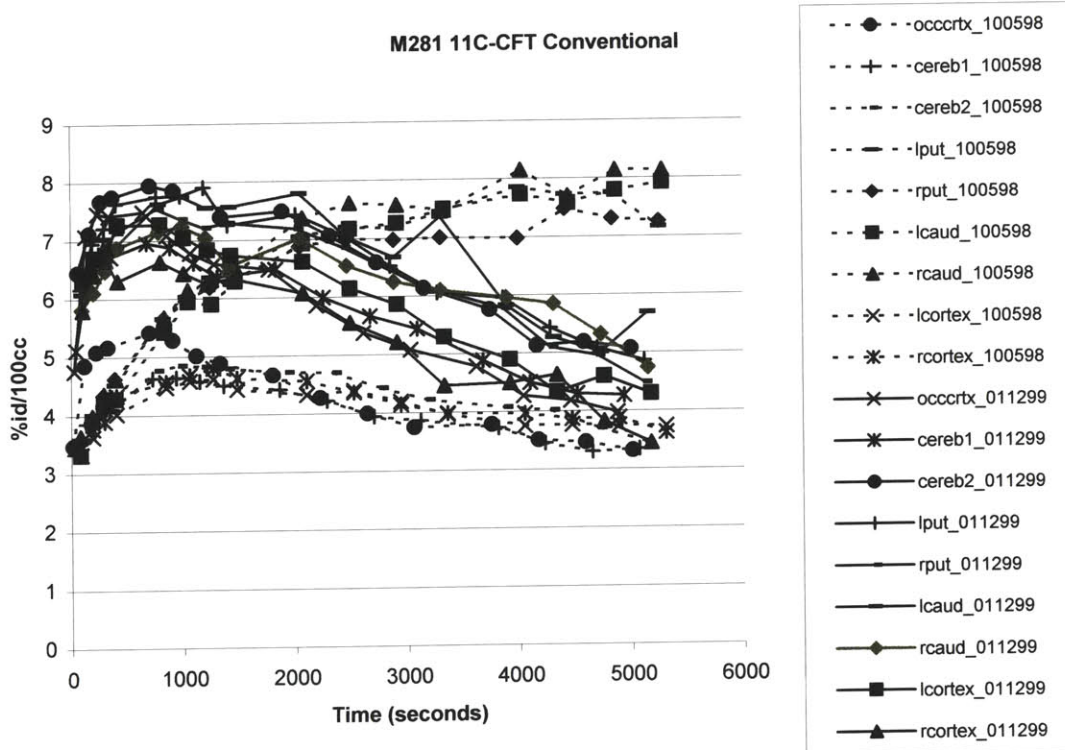


Figure 8. PET studies of  $^{11}\text{C}$ -CFT in a nonhuman primate. 10/05/1998 – before MPTP. 01/12/1999 – after MPTP.

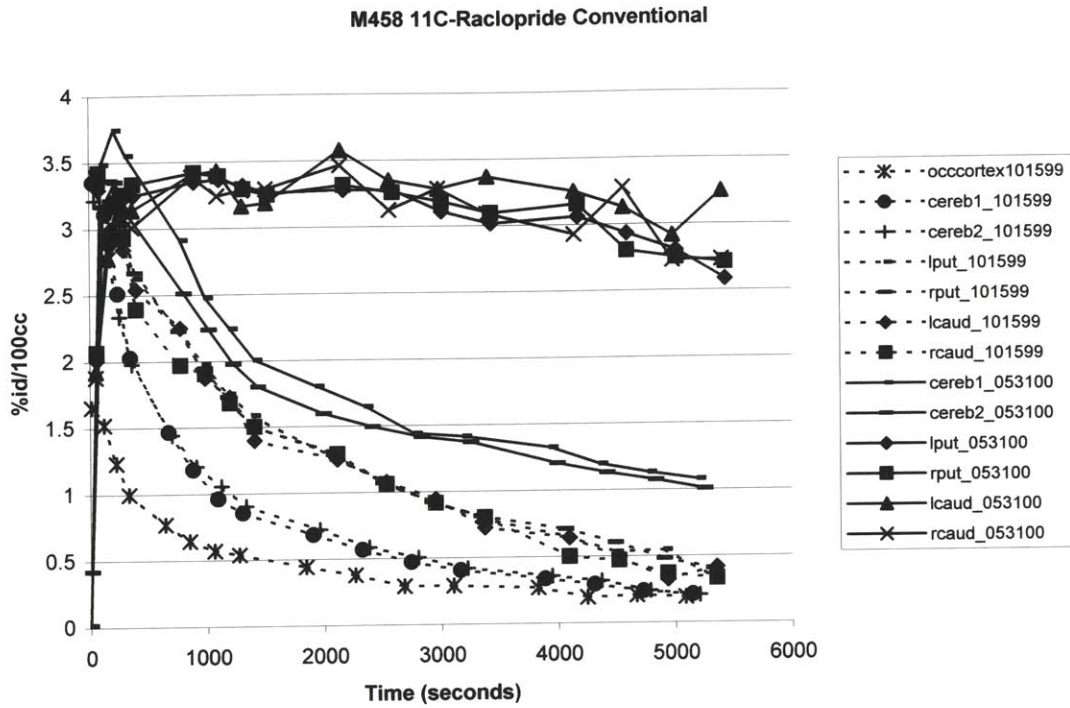


Figure 9. PET studies of  $^{11}\text{C}$ -raclopride in a nonhuman primate. 10/15/1999 – before MPTP. 05/31/2000 – after MPTP.

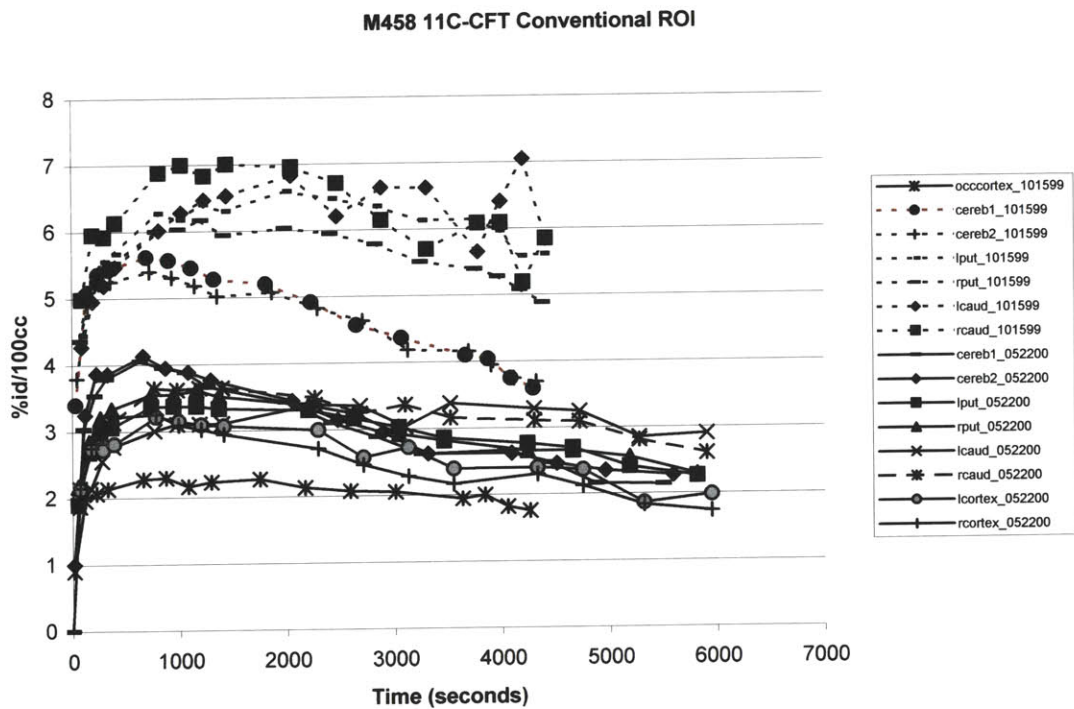


Figure 10. PET studies of  $^{11}\text{C}$ -CFT in a nonhuman primate. 10/15/1999 – before MPTP. 05/22/2000 – after MPTP.

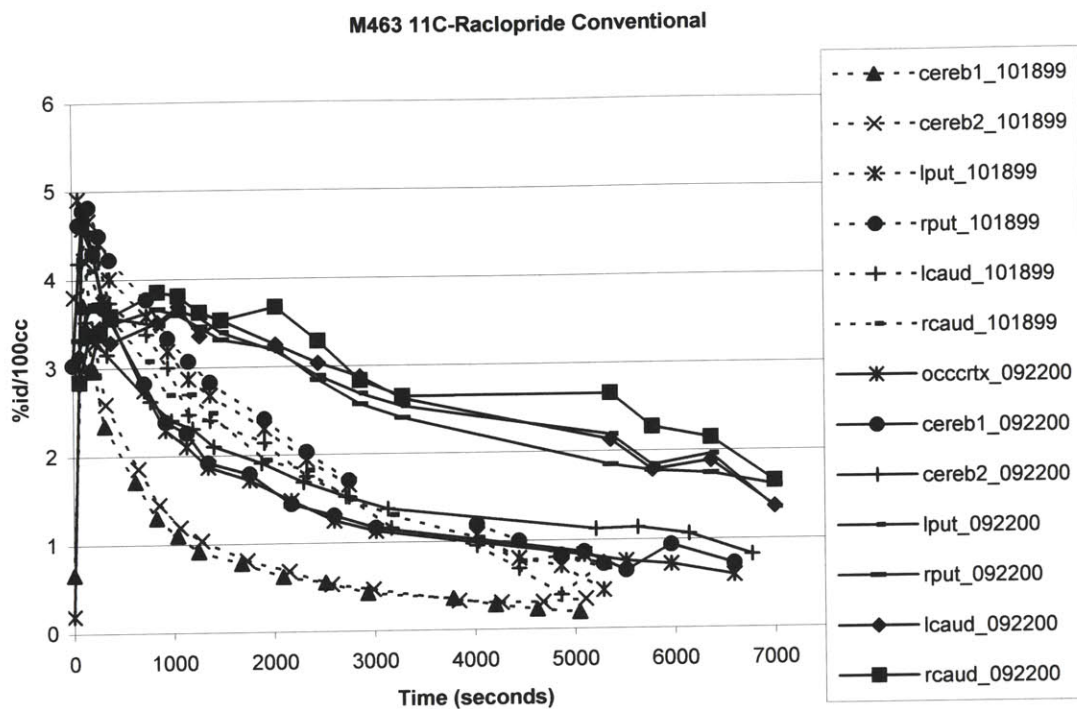


Figure 11. PET studies of  $^{11}\text{C}$ -raclopride in a nonhuman primate. 10/18/1999 – before MPTP. 09/22/2000 –after MPTP.

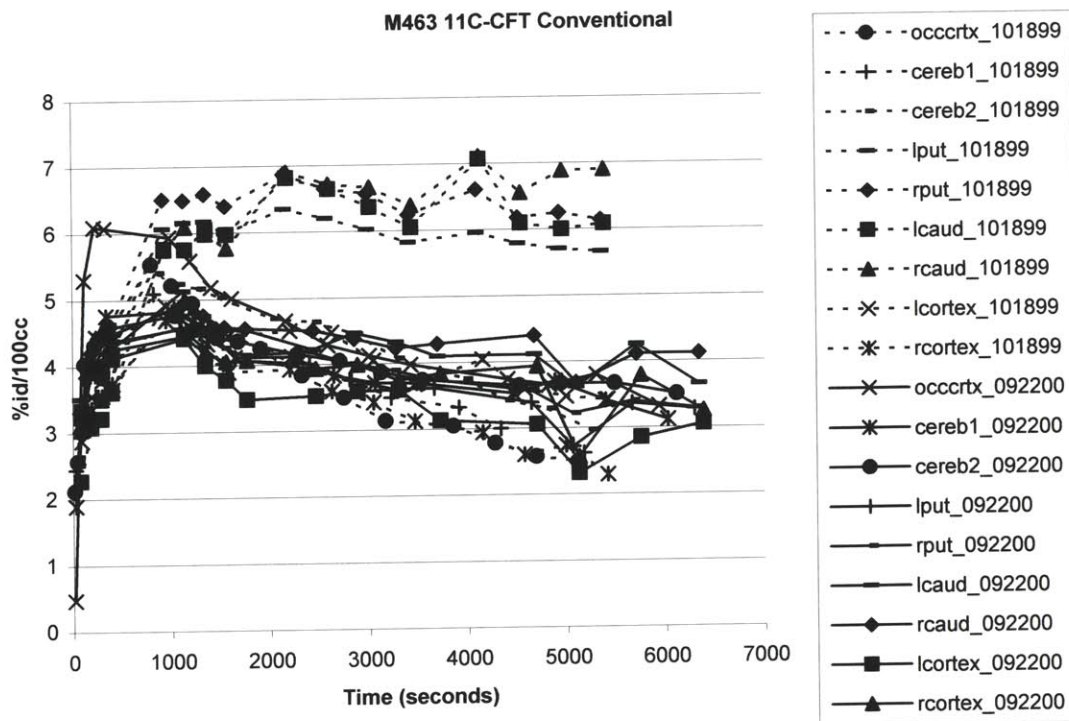


Figure 12. PET studies of  $^{11}\text{C}$ -CFT in a nonhuman primate. 10/18/1999 – before MPTP. 09/22/2000 – after MPTP.

<b>Binding Ratios from Conventional 2D Analysis of <sup>11</sup>C-Raclopride</b>				
	L_Caudate	R_Caudate	L_Putamen	R_Putamen
<b>pre MPTP</b>				
m281 100598	1.7933	2.1594	2.0745	2.0434
m458 101599	0.9028	0.9245	0.9389	0.9402
m463 101899	0.8515	0.8954	1.0466	1.1713
<b>post MPTP</b>				
m281 010599	2.5514	2.744	2.838	2.913
m458 053100	1.1106	1.2219	1.0892	1.1194
m463 092200	1.2238	1.2165	1.1106	1.0107

Table 3. Binding ratios from two-dimensional ROI analysis of <sup>11</sup>C-raclopride data.

<b>Binding Ratios from Conventional 2D Analysis of <sup>11</sup>C-CFT</b>				
	L_Caudate	R_Caudate	L_Putamen	R_Putamen
<b>pre MPTP</b>				
m281 100598	0.8249	0.8862	0.8163	0.7463
m458 101599	0.4646	0.3548	0.4164	0.2738
m463 101899	0.7046	0.7676	0.6151	0.7408
<b>post MPTP</b>				
m281 011299	0.2428	0.1454	0.1601	0.1468
m458 052200	0.1355	0.1347	0.05131	0.0441
m463 092200	0.1475	0.1481	-0.0216	0.0361
<b>Striatal to Cerebellar Ratios from Conventional 2D Analyses of <sup>11</sup>C-CFT - 60 minutes</b>				
	L_Caudate	R_Caudate	L_Putamen	R_Putamen
<b>pre MPTP</b>				
m281 100598	2.008120089	2.060650715	2.017544195	1.844719863
m458 101599	1.379364918	1.484631853	1.498762879	1.316371464
m463 101899	1.736407989	1.831660847	1.671815185	1.790704521
<b>post MPTP</b>				
m281 011299	1.165840355	1.246957398	0.959646709	1.010634125
m458 052200	1.278157942	1.168399237	1.164453475	1.151088904
m463 092200	1.291026913	1.207475598	1.090616847	1.076596064

Table 4. Binding ratios from two-dimensional ROI analysis of <sup>11</sup>C-CFT data.

**Compartmental Modeling Results of Binding Potential from Conventional 2D ROI Analyses of <sup>11</sup>C-Raclopride - k<sub>3</sub>/k<sub>4</sub>**

	L_Caudate	R_Caudate	L_Putamen	R_Putamen
M281 100598 pre MPTP	4.861	5.109	6.338	6.317
M458 101599 pre MPTP	4.665	4.675	4.701	5.004
M458 053100 post MPTP	7.802	3.634	3.900	4.046
M463 092200 post MPTP	2.985	3.459	3.421	3.362

Table 5. Binding potential values ( $k_3/k_4$ ) obtained from tracer kinetic model fits of <sup>11</sup>C-raclopride ROI data in a primate model of Parkinson's disease. A two exponential fit of blood data provides the input function to the tracer kinetic compartmental model.

The binding ratio of <sup>11</sup>C-raclopride is increased by 26 ± 11% post MPTP treatment, indicating significantly enhanced binding to the postsynaptic dopamine D<sub>2</sub> receptors and an upregulation of dopamine D<sub>2</sub> receptors (receptor supersensitivity). The binding ratio of <sup>11</sup>C-CFT to the striatal dopamine transporters is decreased by 82 ± 8% post MPTP treatment, indicating a loss of dopamine transporter sites. As seen from Table 4, <sup>11</sup>C-CFT binding decreases far more strongly in the putamen than in the caudate. This effect is seen in Parkinson's disease in humans and shows the dopamine terminals in the putamen are more sensitive to MPTP than the dopamine terminals in the caudate.

### 6.3 Volumetric Region of Interest Analysis

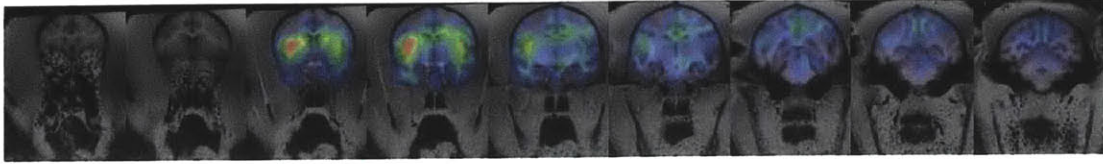
#### 6.3.1 Registration of PET and MRI Data

The corrected image data used in conventional 2D ROI analyses is first repacked using `repack.c` into a dynamic series of sixteen sets of seven stacked slices representing coverage over the brain. The data is then converted into ANALYZE/AVW image format. Each coronal PET image is 5 mm in the axial z direction and 1.19 mm X 1.19

mm in the x-y plane. For an entire study of 128 images the processing ultimately results in 16 X 7 3D volumes for ROI analysis.

T2 weighted MRI data from the same subject with its respective dimensions is then loaded and converted into ANALYZE/AVW image format. The MRI data vary in their dimension according to the imaging machine used (typically either the 1.5 Tesla or the 3.0 Tesla machine located in the NMR Center in Charlestown), but generally consist of 2 mm slices. A segmentation routine in ANALYZE is used on some MRI data to separate the brain from surrounding tissues. The MRI data is then flipped in the x-y direction to match to the PET data. The PET data is finally thresholded (if needed) and coregistered to its respective MRI data using the NMI voxel match algorithm of the ANALYZE software package and cubic spline interpolation. The multimodality image registration routine returns fused PET-MRI images and a transformation matrix that maps the PET images onto the respective MR images. The fused PET-MRI images are then volume rendered for display. Figures 13 and 14 show results from this process.

CFT/m463



Raclopride/m463

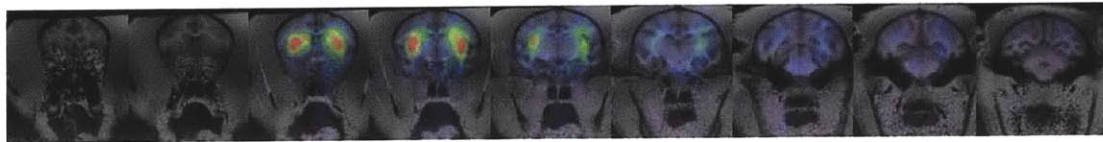


Figure 13. T2 weighted MR images fused with PET images showing dopamine transporter binding ( $^{11}\text{C}$ -CFT) and dopamine  $\text{D}_2$  receptor binding ( $^{11}\text{C}$ -raclopride) in the same primate before MPTP.

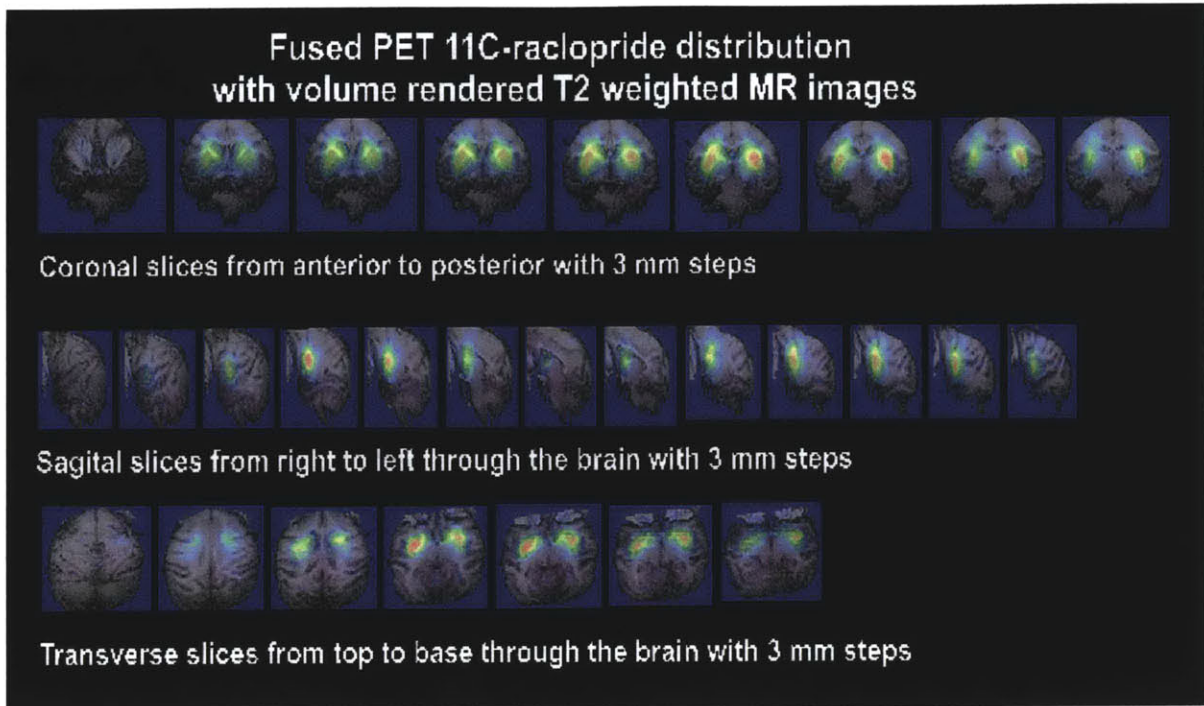


Figure 14. PET study with  $^{11}\text{C}$ -raclopride of dopamine D2 receptors. PET images are fused with volume rendered MR images. The upper row shows coronal slices from anterior to posterior through the monkey brain. Binding to D2 receptors are localized to putamen and caudate. The middle row shows sagittal slices from right to left through the brain. The slices 1-7 represent right hemisphere and slices 8-13 left hemisphere. At the bottom row transverse slices are shown from top to base. Volumetric distribution of radioactivity is used in selecting region (volumes) for interest used in quantitative data analyses of receptor function.

Three-dimensional regions of interest (left and right caudate, right and left putamen, left and right globus pallidus, left and right substantia nigra, thalamus, left and right primary motor cortex, cerebellum, and supplementary motor area) are outlined on the corresponding MR images based on the anatomical borderlines observed from both a primate atlas and the MR images themselves. Figure 15 provides a snapshot of this process.

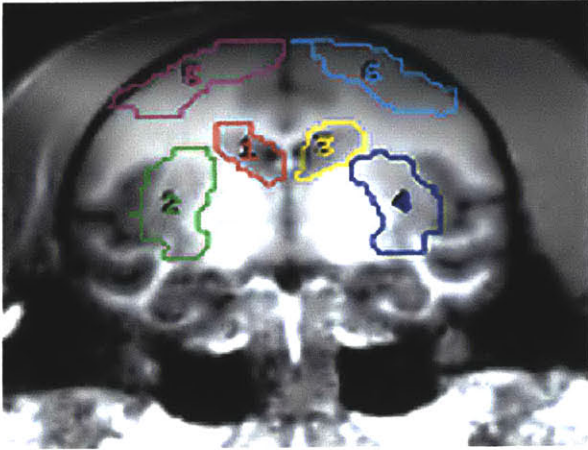


Figure 15. Regions of interest outlined on an MR image for application to its corresponding transformed PET image. Regions 1 and 3 are the right and left caudate; regions 2 and 4 are the right and left putamen; and regions 5 and 6 are the right and left cortex.

The transformation matrix for fusing the PET data to the MRI data is then reapplied to the PET images to generate data for three-dimensional ROI analysis; and activity per unit volume, percent activity of the injected dose and ligand concentration are calculated. The data obtained through ROI analysis is analyzed using a three compartmental model of receptor function and the SAAM II program. The plasma data obtained during each experiment again provides the input functions used to complete the pharmacokinetic and physiological analyses.

### 6.3.2 Time Activity Curves, Analysis and Results

Time activity curves are generated from the volumetric ROI analysis. Results from PET studies of  $^{11}\text{C}$ -raclopride and  $^{11}\text{C}$ -CFT in a MPTP induced primate model of Parkinson's disease are shown in Figures 16,17,18,19,20 and 21. The earlier dates are pre MPTP; later dates are post MPTP treatment. Binding ratios for  $^{11}\text{C}$ -CFT are determined as a ratio of graphically integrated activity concentrations (40-60 minutes) in the region of interest and cerebellum [Binding Ratio = ( $\int\text{ROI} / \int\text{cerebellum} - 1$ )].

Binding ratios for  $^{11}\text{C}$ -raclopride are determined as a ratio of graphically integrated activity concentrations (about the equilibrium point of 40-42 minutes) in the region of interest and cerebellum [ $\text{Binding Ratio} = (\int\text{ROI} / \int\text{cerebellum} - 1)$ ]. The percent difference between the striatum and the cerebellum is then calculated. Results are shown in Tables 6 and 7. Compartmental model fits of  $k_1 - k_4$  using SAAM II were performed, and  $\frac{k_3}{k_4}$  values are shown in Table 8. The blood data is fitted to a biexponential function, which is then used as an input in fitting the time activity curve data to the set of differential equations of the compartmental model.

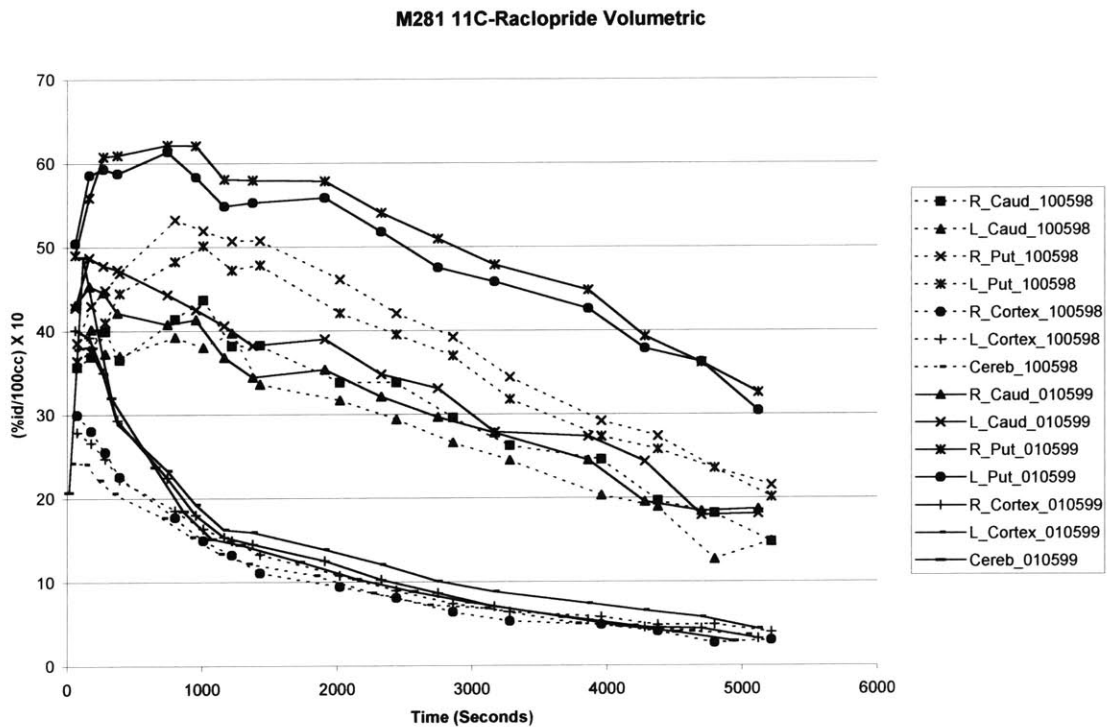


Figure 16. PET studies of  $^{11}\text{C}$ -raclopride in a nonhuman primate. 10/05/1998 – before MPTP. 01/05/1999 – after MPTP. Volumetric regions of interest were used to produce the time activity curves.

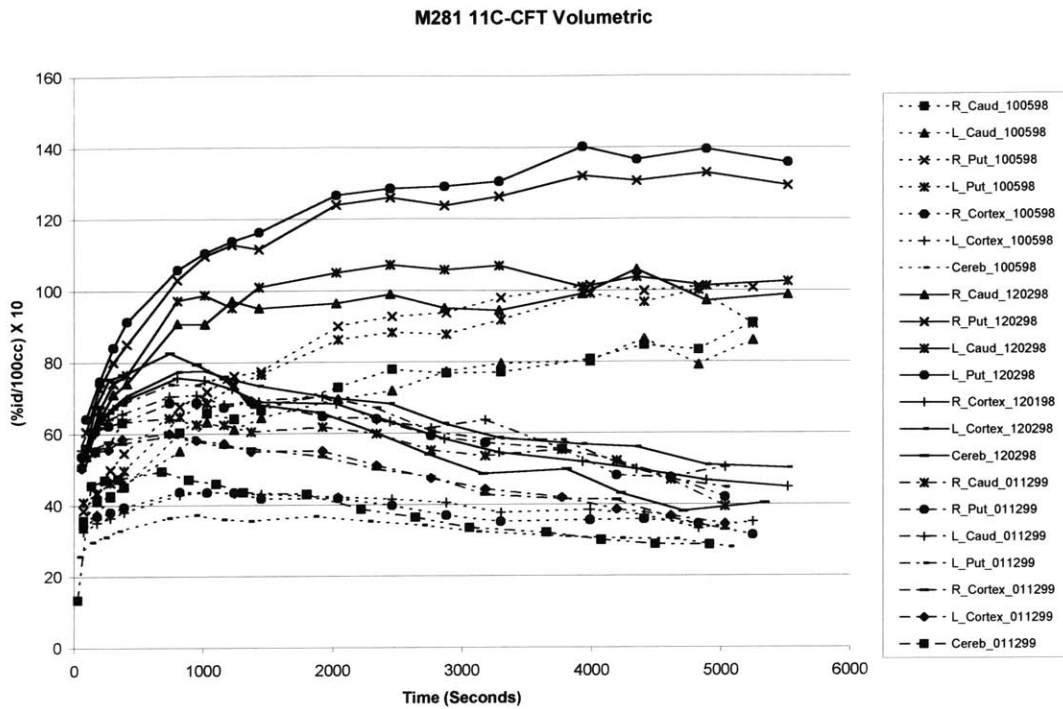


Figure 17. PET studies of  $^{11}\text{C}$ -CFT in a nonhuman primate. 10/05/1998 – before MPTP. 12/02/1998 and 01/12/1999 – after MPTP. Volumetric regions of interest were used to produce the time activity curves.

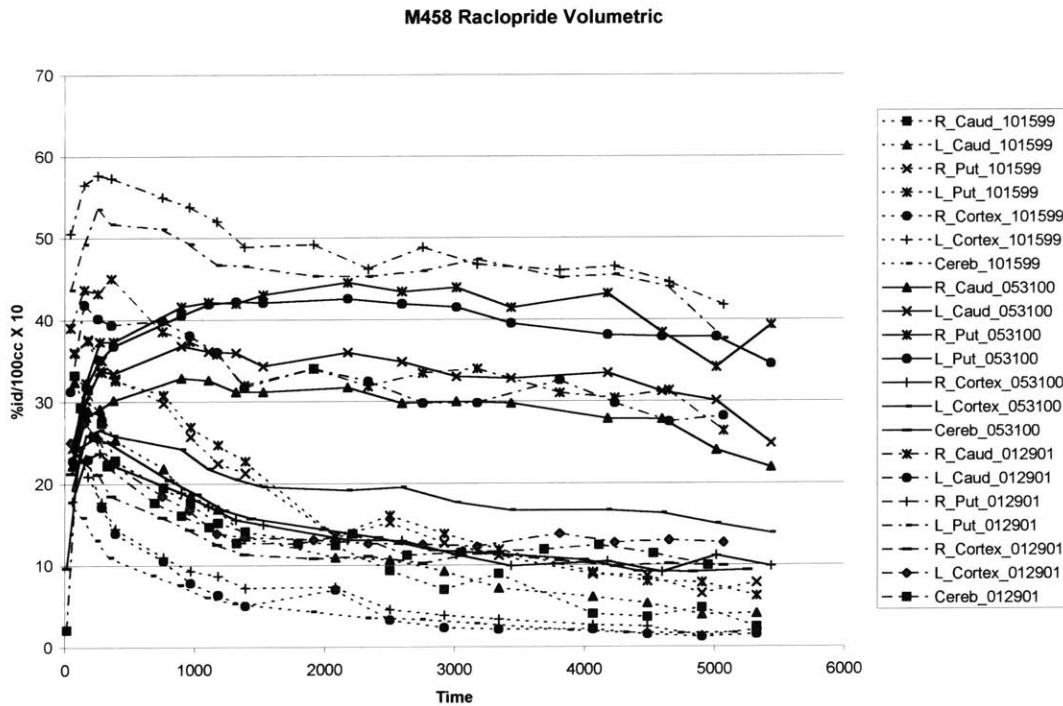


Figure 18. PET studies of  $^{11}\text{C}$ -raclopride in a nonhuman primate. 10/15/1999 – before MPTP. 05/31/2000 and 01/29/2001 – after MPTP. Volumetric regions of interest were used to produce time activity curves. Note overall decrease of accumulation in all brain areas for M458 after MPTP for both  $^{11}\text{C}$ -raclopride and of  $^{11}\text{C}$ -CFT.

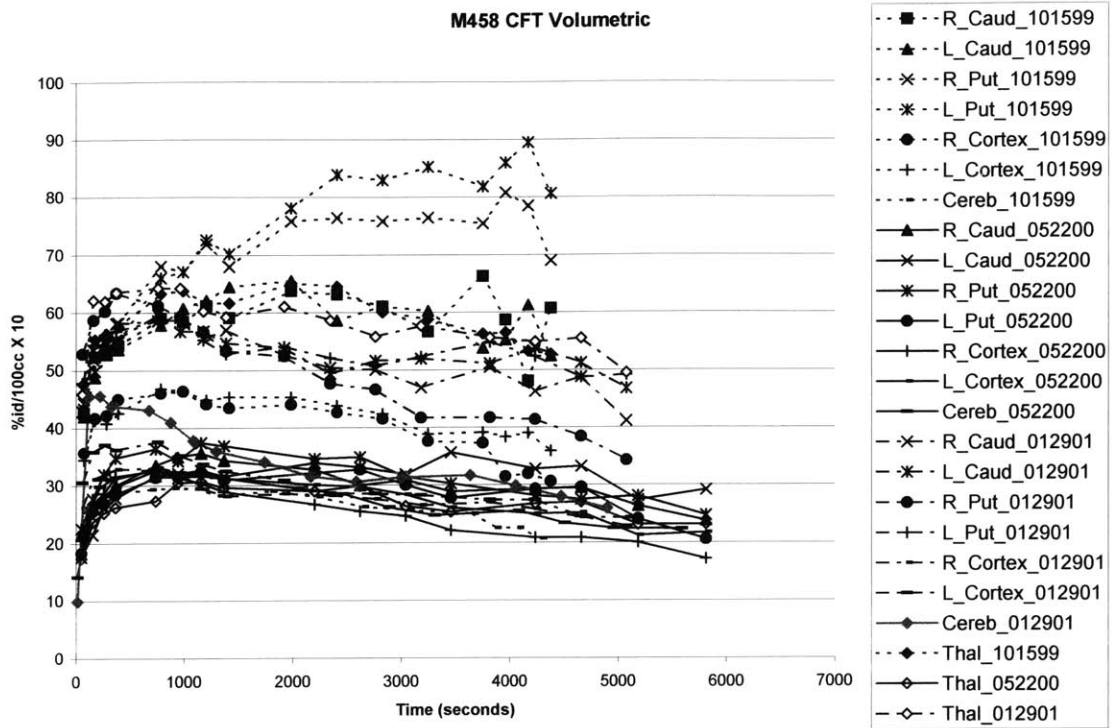


Figure 19. PET studies of <sup>11</sup>C-CFT in a nonhuman primate. 10/15/1999 – before MPTP. 05/22/2000 and 01/29/2001 – after MPTP. Volumetric regions of interest were used to produce time activity curves.

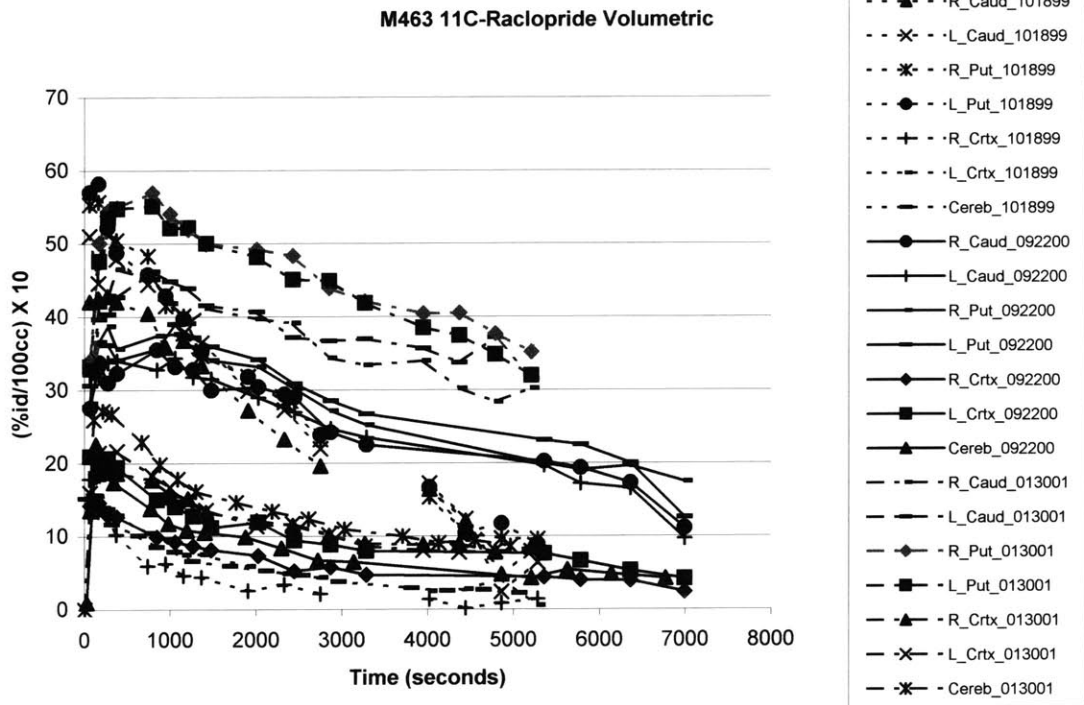


Figure 20. PET studies of <sup>11</sup>C-raclopride in a nonhuman primate. 10/18/1999 – before MPTP. 09/22/2000 and 01/30/2001 – after MPTP. Volumetric regions of interest were used to produce time activity curves.

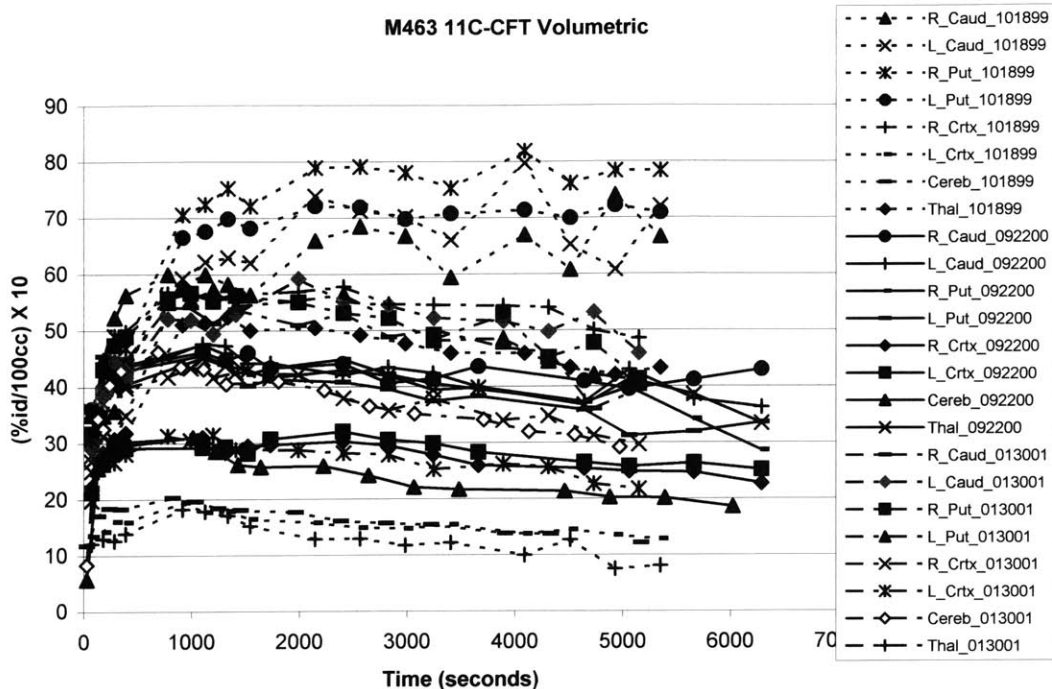


Figure 21. PET studies of <sup>11</sup>C-CFT in a primate. 10/18/1999 – before MPTP. 09/22/2000 and 01/30/2001 – after MPTP. Volumetric regions of interest were used to generate the time activity curves.

Binding Ratios from Volumetric 3D Analysis of <sup>11</sup> C-Raclopride										
	L_Caud	R_Caud	L_Put	R_Put	L_GP	R_GP	L_SMA	R_SMA	L_SN	R_SN
<b>pre MPTP</b>										
m281 100598	1.9822	2.2483	2.9334	3.2197	---	---	---	---	---	---
m458 101599	1.4393	1.4915	2.841	2.625	1.6189	1.2318	0.358	0.2075	0.7294	0.3046
m463 101899	3.641	3.2654	3.8033	3.5651	2.9396	3.2962	0.7925	0.8089	0.3803	0.25
m476 101800	1.5737	1.1952	2.0458	2.282	1.2605	1.2169	0.7396	0.6326	0.25084	0.2287
<b>post MPTP</b>										
m281 010599	1.9021	1.6881	3.2126	3.412	---	---	---	---	---	---
m458 053100	1.8084	1.4039	2.3791	2.5909	1.4138	1.5699	-0.1801	-0.167	0.235	0.1086
m458 012901	1.2172	1.2933	2.2235	2.5792	1.4046	1.5434	-0.0217	-0.1686	0.4282	0.2685
m463 092200	2.9016	2.8475	3.5058	3.1565	3.0121	2.641	0.7324	0.3383	0.7348	0.8124
m463 013001	2.2906	2.0599	2.7693	2.8049	2.3689	2.377	0.0539	0.143	0.9554	0.4279
m464 111700	1.5464	1.5536	2.0008	1.933	1.5357	1.6212	0.4104	0.5744	0.3889	0.3989

Table 6. Binding ratios from three-dimensional ROI analysis of <sup>11</sup>C-raclopride data. L\_Caud is the left caudate, R\_Caud is the right caudate, L\_Put is the left putamen, R\_Put is the right putamen, L\_GP is the left globus pallidus, R\_GP is the right globus pallidus, L\_SMA is the left supplementary motor area, R\_SMA is the right supplementary motor area, L\_SN is the left substantia nigra, R\_SN is the right substantia nigra.

Binding Ratios from Volumetric 3D Analysis of <sup>11</sup> C-CFT									
	L_Caud	R_Caud	L_Put	R_Put	L_GP	R_GP	L_SMA	R_SMA	Thal
<b>pre MPTP</b>									
m281 100598	1.2458	1.2748	1.6281	1.7918	---	---	---	---	---
m458 101599	1.2275	1.2638	1.8510	1.7613	1.2947	1.3311	0.2260	0.2484	1.2767
m463 101899	3.4037	3.1292	3.5074	3.9310	3.0059	3.6318	0.1929	0.2857	2.0303
m476 101800	1.3127	1.0454	1.6499	1.5525	0.9990	0.9677	0.7816	0.8481	---
<b>post MPTP</b>									
m281 011299	0.6866	0.6097	0.7349	0.7702	---	---	---	---	---
m458 052200	0.2773	0.1621	0.2123	0.2513	0.0705	0.1623	0.0160	-0.0043	0.0267
m458 012901	0.9329	0.8168	1.0754	0.7067	1.4137	1.2540	0.0146	0.0107	1.1116
m463 092200	0.7876	0.8074	0.6622	0.7801	0.7160	0.8614	0.5336	0.5787	0.7489
m463 013001	0.4698	0.3697	0.4144	0.4206	0.5650	0.4383	0.0816	0.1738	0.5245
m464 111700	1.4737	1.1210	1.3735	1.4093	1.2213	1.3633	0.9958	1.0646	---
m464 040901	0.4261	0.3432	0.4618	0.4871	0.6276	0.6059	0.3010	0.2516	---

Table 7. Binding ratios from three-dimensional ROI analysis of <sup>11</sup>C-CFT data.

Compartmental Modeling Results of Binding Potential from Volumetric 3D ROI Analyses of <sup>11</sup> C-Raclopride - k <sub>3</sub> /k <sub>4</sub>										
	L_Caud	R_Caud	L_Put	R_Put	L_GP	R_GP	L_PMC	R_PMC	L_SMA	R_SMA
<b>pre MPTP</b>										
M281 100598	2.8260	3.2035	6.4727	8.1512	---	---	0.5112	0.5709	---	---
<b>post MPTP</b>										
M458 053100	8.2791	6.6085	10.1594	11.8600	9.0244	7.0411	5.6994	5.4790	5.2306	5.2068
M463 092200	4.0868	4.0868	4.71865	3.98843	3.4979	4.0266	1.6949	1.1683	2.4083	1.9287

Table 8. Binding potential values (k<sub>3</sub>/k<sub>4</sub>) obtained from tracer kinetic model fits of <sup>11</sup>C-raclopride ROI data in a primate model of Parkinson's disease.

The binding ratio of <sup>11</sup>C-raclopride in the striatum is decreased by 9 ± 3% post MPTP treatment using this form of analysis. The binding ratio of <sup>11</sup>C-CFT to the striatal dopamine transporters is decreased by 65 ± 6% post MPTP treatment, indicating a loss of dopamine transporter sites. This result is in close agreement with published results.

As seen from Table 7,  $^{11}\text{C}$ -CFT binding tends to decrease more strongly in the putamen than in the caudate. From volumetric analysis it is again seen that the dopamine terminals in the putamen are more sensitive to MPTP than the dopamine terminals in the caudate; however, dopamine  $\text{D}_2$  receptor supersensitivity, which leads to an upregulation of  $\text{D}_2$  receptors and increased binding ratios, is not observed as one would expect. This result is explained by a combination of two factors: 1) coregistration errors may exist in the axial z direction, and a loss of information in PET data may result from the use of cubic spline interpolation; 2) two-dimensional PET analysis permits analysis only in areas of high receptor density, and underlying tissue may have different receptor densities. For all coregistrations performed in this thesis, the axial coregistration error in the z direction is the greatest source of error. The error results from the fact that the entire brain is not covered in the range of PET scans performed for each experiment, so that a 10 mm gap is left between the cerebellar and striatal areas for fusion. The result is that cerebellar percent activity of injected dose is lower than that obtained through standard two dimensional analyses, leading to higher pre MPTP binding ratios and higher rate constants both pre MPTP and post MPTP for compartmental tracer kinetic model fits.

#### **6.4 Bayesian MAP Reconstruction**

The Bayesian MAP iterative coordinate descent reconstruction algorithm and an rpm package for a libc5 gcc compiler were both downloaded and installed on the RedHat Linux 6.1 platform. The Bayesian reconstruction algorithm uses Matlab for both input and output. Code for PCR-I was modified to dump attenuation corrected sinogram data

into a format, which was then read into Matlab and saved for reconstruction along with the needed PCR-I specifications. The number of projection angles, the number of displacements, the projection spacing, the angular projection spacing, displacement of first projection, first projection angle, and a scatter value of zero are added to the attenuation corrected sinogram data in Matlab format (\*.mat). The following PCR-I values were determined for input into the reconstruction algorithm:

Number of displacements: 145

Number of projection angles: 180

Projection spacing: 1.824 mm

Angular projection spacing: 0.0175 radians

Displacement of first projection: -131.3280 degrees

First projection angle: 0 degrees

The reconstruction algorithm can be initialized with convolution backprojection reconstructions; however, since images reconstructed by this method are set at a nonstandard resolution of 159 by 159 pixels, this method was not chosen. Instead, no initializations were applied to this algorithm. The scale parameter  $s$  for the prior model is set at 1.0; the shape parameter  $p$  of the prior model is set at 2.0; and the field of view is set at 400 mm. The final size of the images reconstructed with this algorithm is set at 256 by 256 pixels.

After reconstruction the images are corrected for decay, camera calibration, and collection time using scripts and a series of programs written in C.

#### **6.4.1 Registration of PET and MRI Data**

After correction the image data is repacked using `repack.c` into a dynamic series of sixteen sets of seven stacked slices representing coverage over the brain. The data is then converted into ANALYZE/AVW image format. Each coronal PET image is 5 mm in the axial z direction and 0.739 mm X 0.739 mm in the x-y plane. For an entire study of 128 images the processing ultimately results in 16 X 7 3D volumes for ROI analysis.

T2 weighted MRI data from the same subject with its respective dimensions is then loaded and converted into ANALYZE/AVW image format. The MRI data vary in their dimension according to the imaging machine used (typically either the 1.5 Tesla or the 3.0 Tesla machine located in the NMR Center in Charlestown), but generally consist of 2 mm slices. A segmentation routine in ANALYZE is used on some MRI data to separate the brain from surrounding tissues. The MRI data is then flipped in the x-y direction to match to the PET data. The PET data is finally thresholded (if needed) and coregistered to its respective MRI data using the NMI voxel match algorithm of the ANALYZE software package and cubic spline interpolation. The multimodality image registration routine returns fused PET-MRI images and a transformation matrix that maps the PET images onto the respective MR images. The fused PET-MRI images are then volume rendered for display. Figures 22 and 23 show results from this process.

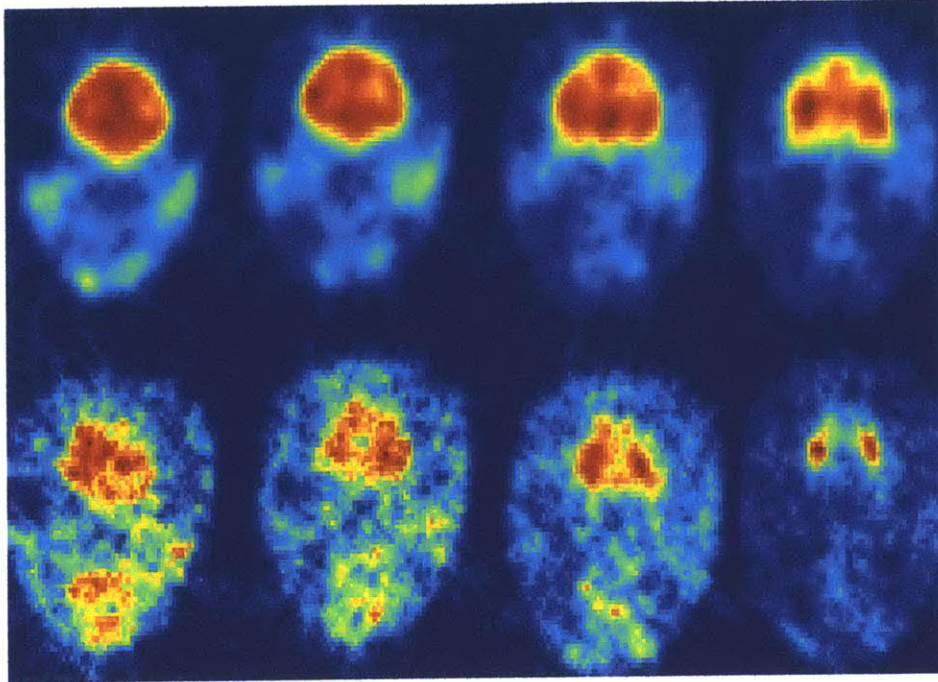


Figure 22. PET studies of dopamine D2 receptors using  $^{11}\text{C}$ -raclopride and dopamine transporters using  $^{11}\text{C}$ -CFT in the same nonhuman primate before MPTP neurotoxicity. The PET images are reconstructed using Bayesian MAP with iterative coordinate descent.

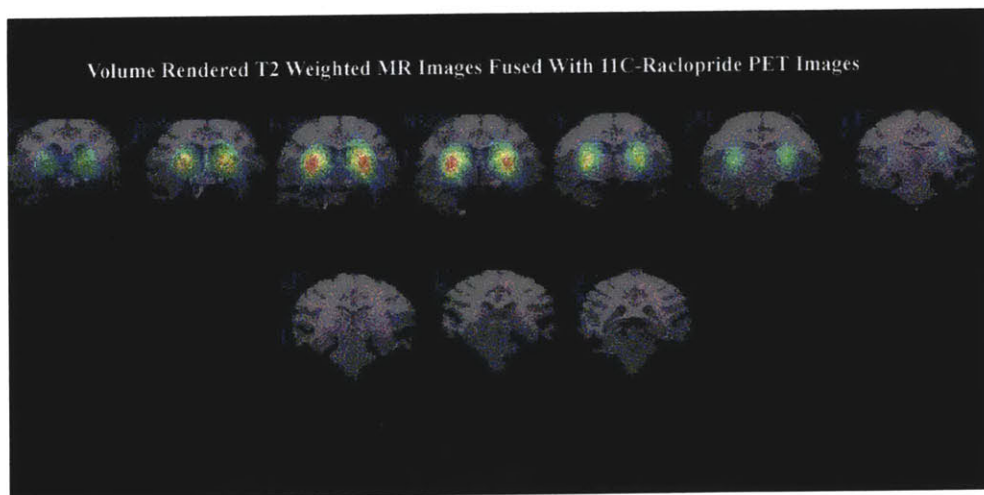


Figure 23. PET study of dopamine D2 receptors using  $^{11}\text{C}$ -raclopride. PET images are reconstructed using Bayesian MAP ICD and fused with volume rendered MR images. The upper row shows coronal slices from anterior to posterior through the monkey brain. Binding to D2 receptors are localized to putamen and caudate. Volumetric distribution of radioactivity is used in selecting region (volumes) for interest used in quantitative data analyses of receptor function. Coronal slices are from anterior to posterior with approximately 3 mm steps.

#### 6.4.2 Time Activity Curves, Analysis and Results

Time activity curves are generated from volumetric ROI analysis and conventional 2D ROI analysis. Results from PET studies of  $^{11}\text{C}$ -raclopride and  $^{11}\text{C}$ -CFT in a MPTP induced primate model of Parkinson's disease are shown in Figures 24 and 25. The earlier dates are pre MPTP; later dates are post MPTP treatment. Binding ratios for  $^{11}\text{C}$ -CFT are determined as a ratio of graphically integrated activity concentrations (40-60 minutes) in the region of interest and cerebellum [Binding Ratio =  $(\int\text{ROI} / \int\text{cerebellum} - 1)$ ]. Binding ratios for  $^{11}\text{C}$ -raclopride are determined as a ratio of graphically integrated activity concentrations (about the equilibrium point of 40-42 minutes) in the region of interest and cerebellum [Binding Ratio =  $(\int\text{ROI} / \int\text{cerebellum} - 1)$ ]. The percent difference between the striatum and the cerebellum is then calculated. Results are shown in Tables 9 and 10. Compartmental model fits of  $k_1 - k_4$  were performed and  $\frac{k_3}{k_4}$  values for a conventional 2D ROI analysis are shown in Table 11. Blood data is fitted to a biexponential function, which is then used as an input in fitting the time activity curve data to the set of differential equations of the compartmental model.

11C-Raclopride M458 Bayesian

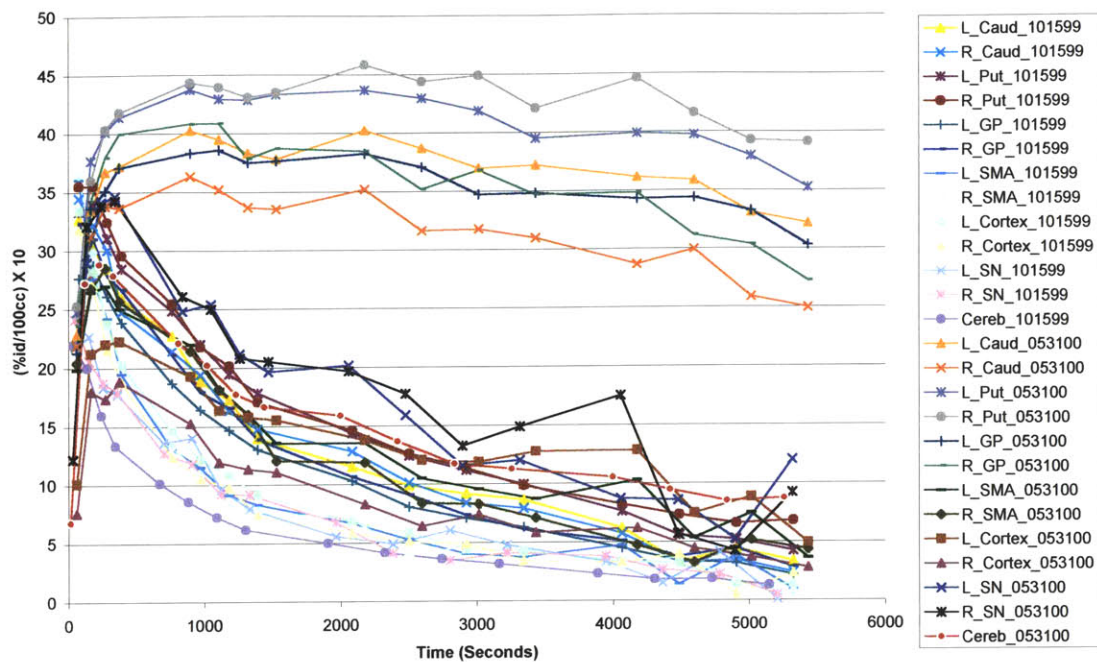


Figure 24. PET studies of <sup>11</sup>C-raclopride in a nonhuman primate. 10/15/1999 – before MPTP. 05/31/2000 and 01/29/2001 – after MPTP. Volumetric regions of interest are utilized to produce time activity curves.

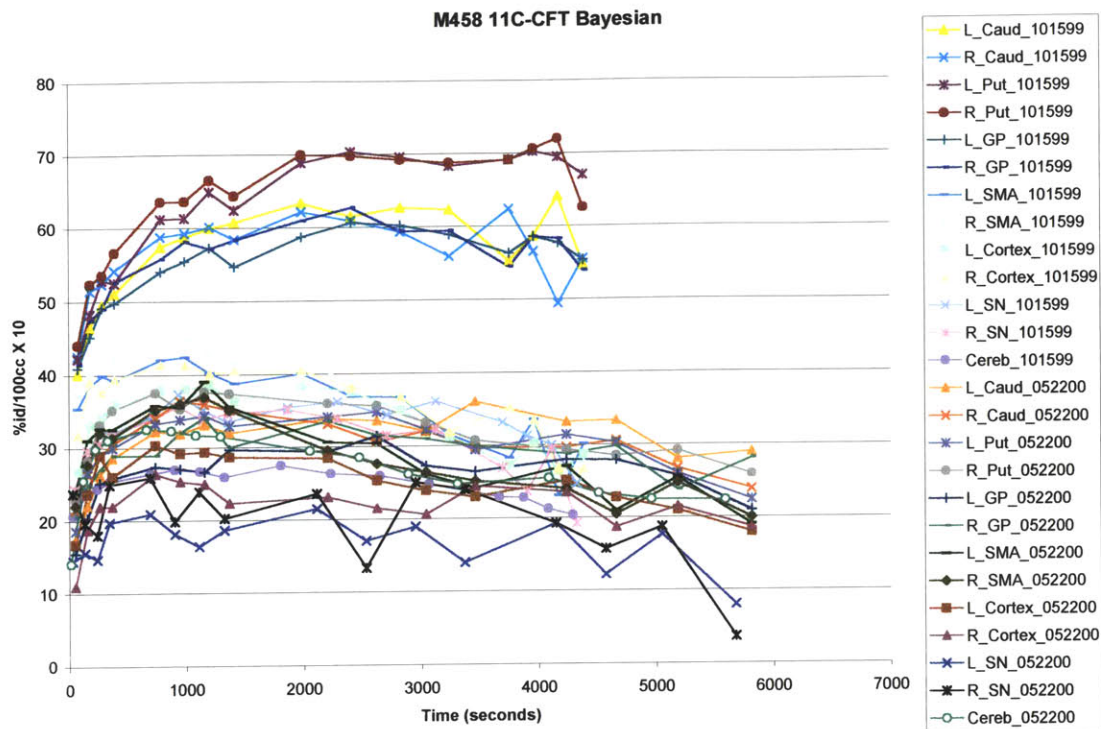


Figure 25. PET studies of <sup>11</sup>C-CFT in a nonhuman primate. 10/15/1999 – before MPTP. 05/22/2000 and 01/29/2001 – after MPTP. Volumetric regions of interest are used to generate the time activity curves.

Binding Ratios from Volumetric 3D Analysis of <sup>11</sup> C-Raclopride											
		L_Caud	R_Caud	L_Put	R_Put	L_GP	R_GP	L_SMA	R_SMA	L_SN	R_SN
<b>pre MPTP</b>											
m458	101599	1.4461	1.3819	2.0331	2.0755	0.94376	1.1122	0.1944	0.1048	0.4047	-0.02748
<b>post MPTP</b>											
m458	053100	1.9805	1.4975	2.3413	2.5158	1.8275	1.8351	-0.2094	-0.3432	0.08174	0.2213

Table 9. Binding ratios from three-dimensional ROI analysis of <sup>11</sup>C-raclopride data. L\_Caud is the left caudate, R\_Caud is the right caudate, L\_Put is the left putamen, R\_Put is the right putamen, L\_GP is the left globus pallidus, R\_GP is the right globus pallidus, L\_SMA is the left supplementary motor area, R\_SMA is the right supplementary motor area, L\_SN is the left substantia nigra, R\_SN is the right substantia nigra.

<b>Binding Ratios from Volumetric 3D Analysis of <sup>11</sup>C-CFT</b>											
		L_Caud	R_Caud	L_Put	R_Put	L_GP	R_GP	L_SMA	R_SMA	L_SN	R_SN
<b>pre MPTP</b>											
m458	101599	1.3918	1.2821	1.6525	1.6582	1.2832	1.3217	0.3883	0.4307	0.3590	0.2697
<b>post MPTP</b>											
m458	052200	0.2773	0.1621	0.2123	0.2513	0.0705	0.1623	0.0160	-0.0043	-0.3708	-0.2157

Table 10. Binding ratios from three-dimensional ROI analysis of <sup>11</sup>C-CFT data.

<b>Compartmental Modeling Results of Binding Potential from Volumetric 2D ROI Analysis of <sup>11</sup>C-Raclopride - k<sub>3</sub>/k<sub>4</sub></b>					
		L_Caud	R_Caud	L_Put	R_Put
<b>post MPTP</b>					
M463	092200	4.5950	3.8689	4.67593	4.48571

Table 11. Binding potential values ( $k_3/k_4$ ) obtained from tracer kinetic model fits of <sup>11</sup>C-raclopride ROI data in a primate model of Parkinson's disease.

The binding ratio of <sup>11</sup>C-raclopride in the striatum is increased by 20% post MPTP treatment using this form of analysis. The binding ratio of <sup>11</sup>C-CFT to the striatal dopamine transporters is decreased by 85% post MPTP treatment, indicating a loss of dopamine transporter sites.

## 6.5 Parametric Imaging Analysis

### 6.5.1 Algorithm

Original code written in Matlab utilizing a genetic algorithm for parametric imaging was modified to handle a biexponential plasma forcing function input. An implementation of the DIRECT algorithm, written in Matlab, for the TOMLAB environment by Mattias Bjorkman of the Department of Mathematics and Physics at

Malardalen University was used to replace the optimization engine. Images reconstructed using convolution backprojection are processed with a Hanning filter and a cutoff value of 0.8. All reconstructed images are filtered using a Weiner filter to further reduce noise.

### 6.5.2 Results

Parametric images were generated for both convolution backprojection and Bayesian MAP methods, producing images of  $k_1, k_2, k_3, k_4$ , and binding potential ( $\frac{k_3}{k_4}$ ).

A mask was applied to the dynamic image sequence to define areas for computation. Parametric imaging results are shown in Figures 26, 27, 28, 29, 30, 31, 32 and 33. The images are converted from Matlab format to ANALYZE format; and regions of interest (including left and right caudate and left and right putamen) are outlined from anatomical representations on the screen in ANALYZE to determine the binding potential ( $\frac{k_3}{k_4}$ ) in areas of interest. Table 12 shows the binding potentials obtained through use of the DIRECT algorithm. These results agree well with those results obtained through traditional tracer kinetic compartmental fits of two-dimensional ROI data and demonstrate the success of the method.

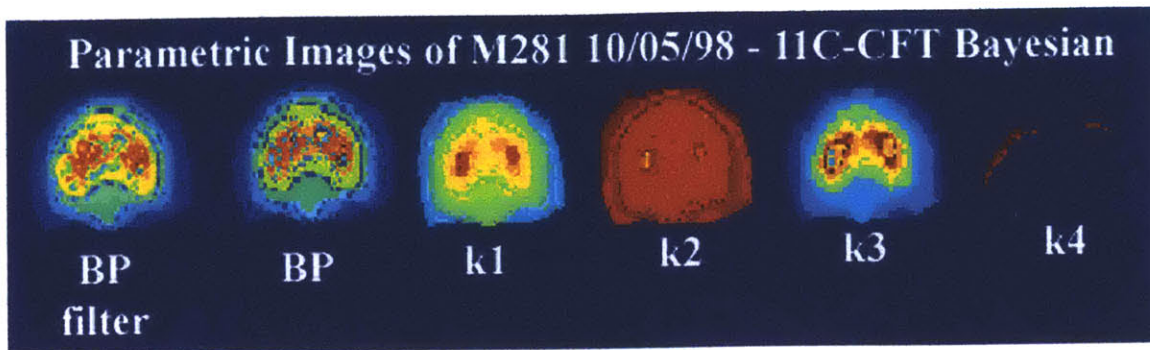


Figure 26. Parametric images of M281  $^{11}\text{C}$ -CFT, pre MPTP treatment. Dynamic image sequence reconstructed by Bayesian MAP algorithm. BP is the resulting parametric image of binding potential; BP filter is a parametric image of the binding potential that has been anisotropically filtered.

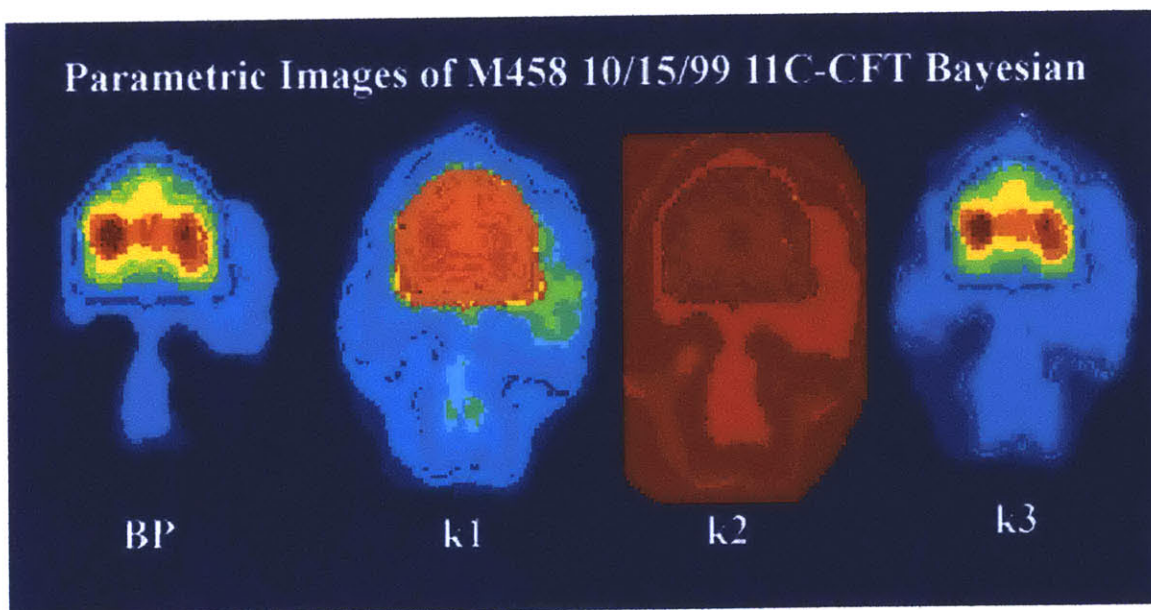


Figure 27. Parametric images of M458  $^{11}\text{C}$ -CFT, pre MPTP treatment. Dynamic image sequence reconstructed by Bayesian MAP algorithm.

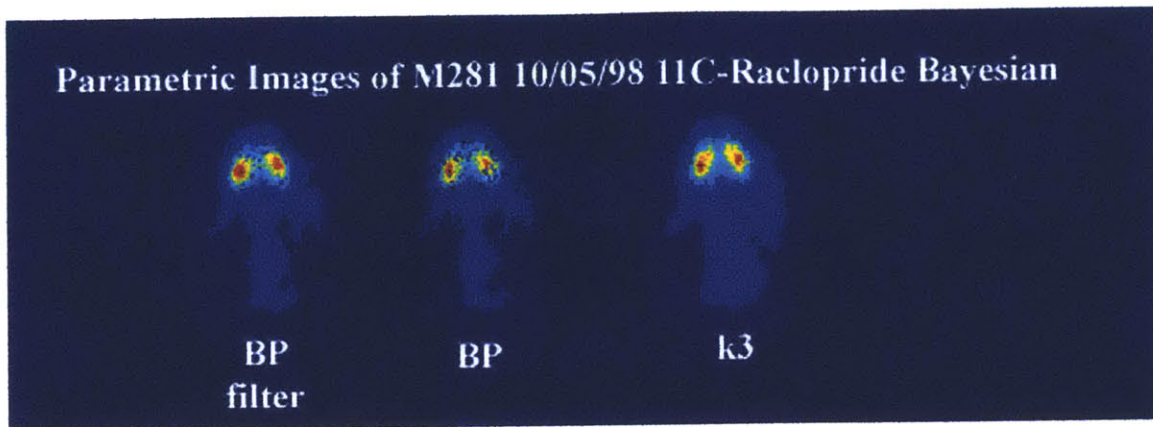


Figure 28. Parametric images of M281  $^{11}\text{C}$ -Raclopride, pre MPTP treatment. Dynamic image sequence reconstructed by Bayesian MAP algorithm. BP is the resulting parametric image of binding potential; BP filter is a parametric image of the binding potential that has been anisotropically filtered.

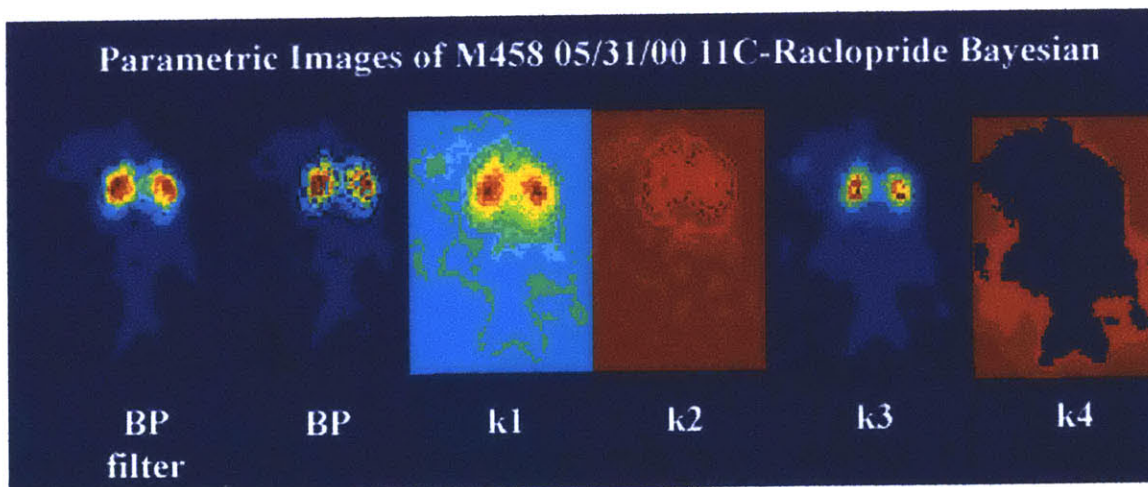


Figure 29. Parametric images of M458  $^{11}\text{C}$ -Raclopride, post MPTP treatment. Dynamic image sequence reconstructed by Bayesian MAP algorithm. BP is the resulting parametric image of binding potential; BP filter is a parametric image of the binding potential that has been anisotropically filtered.

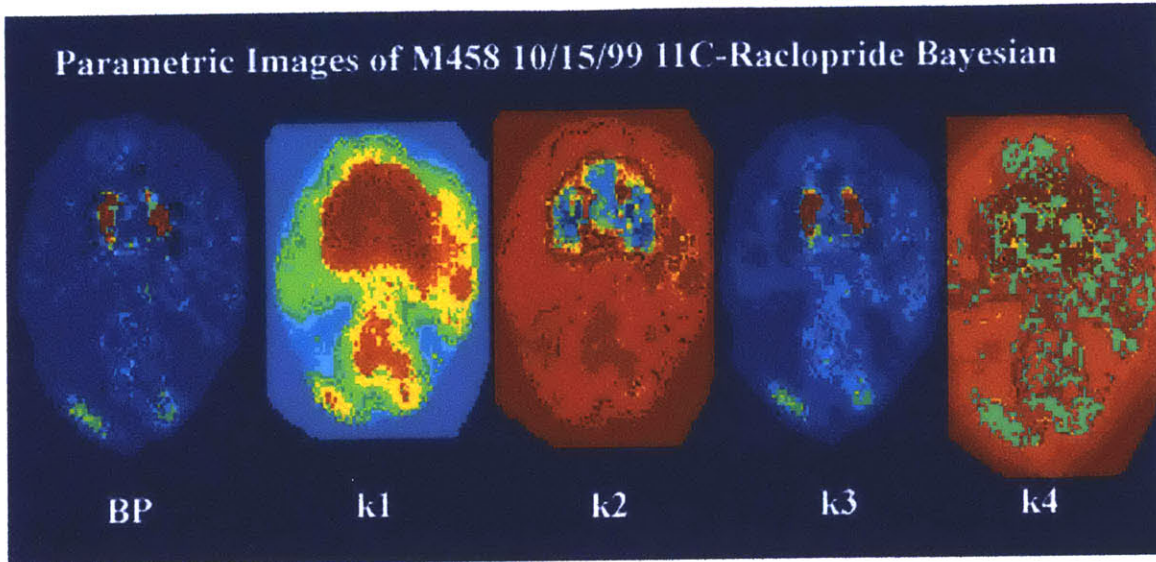


Figure 30. Parametric images of M458  $^{11}\text{C}$ -Raclopride, pre MPTP treatment. Dynamic image sequence reconstructed by Bayesian MAP algorithm.

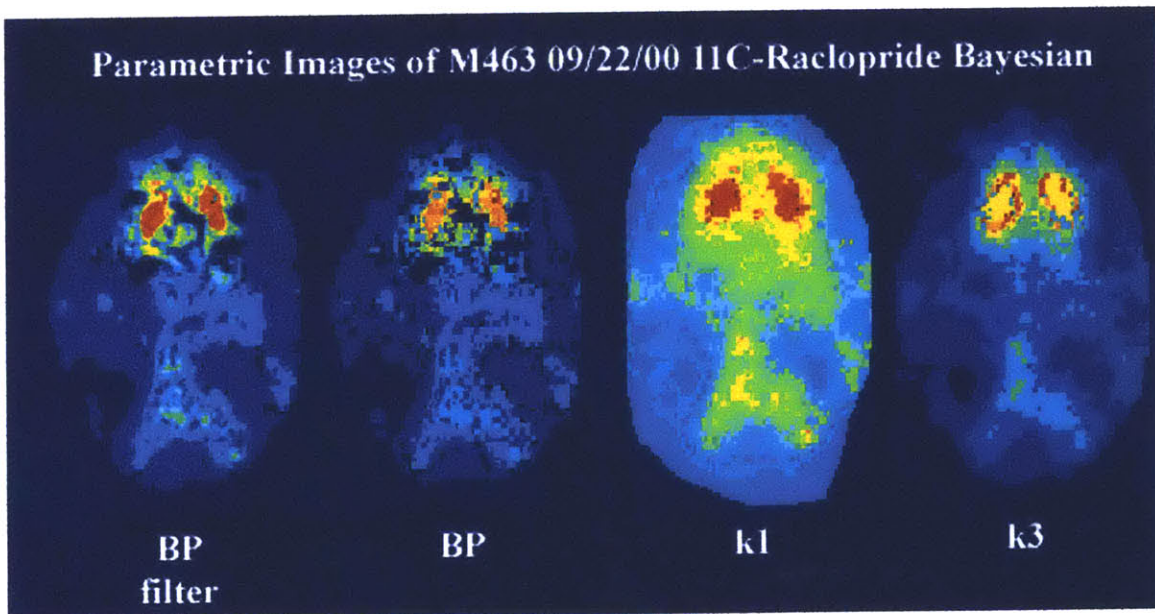


Figure 31. Parametric images of M463  $^{11}\text{C}$ -Raclopride, post MPTP treatment. Dynamic image sequence reconstructed by Bayesian MAP algorithm. BP is the resulting parametric image of binding potential; BP filter is a parametric image of the binding potential that has been anisotropically filtered.

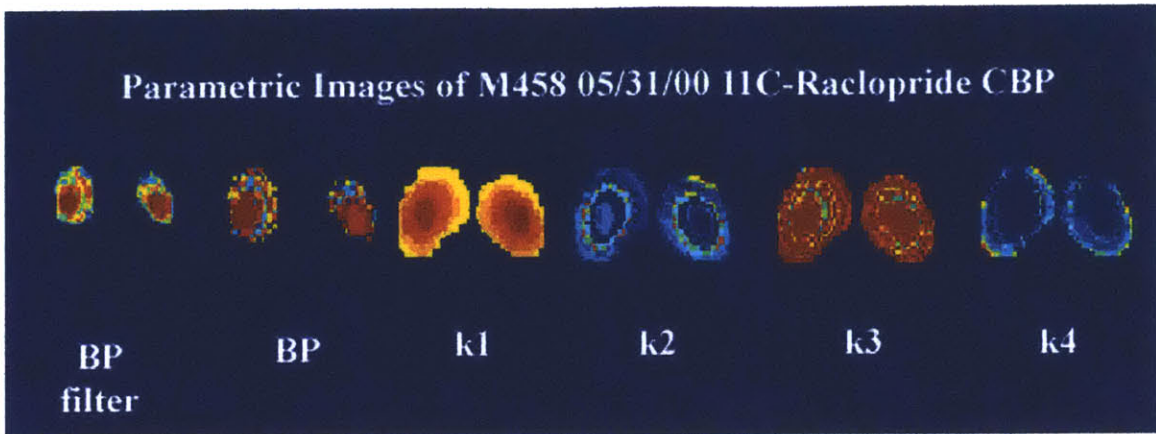


Figure 32. Parametric images of M458  $^{11}\text{C}$ -Raclopride, post MPTP treatment. Dynamic image sequence reconstructed by Hanning weighted convolution backprojection with a cutoff value of 0.8. BP is the resulting parametric image of binding potential; BP filter is a parametric image of the binding potential that has been anisotropically filtered.

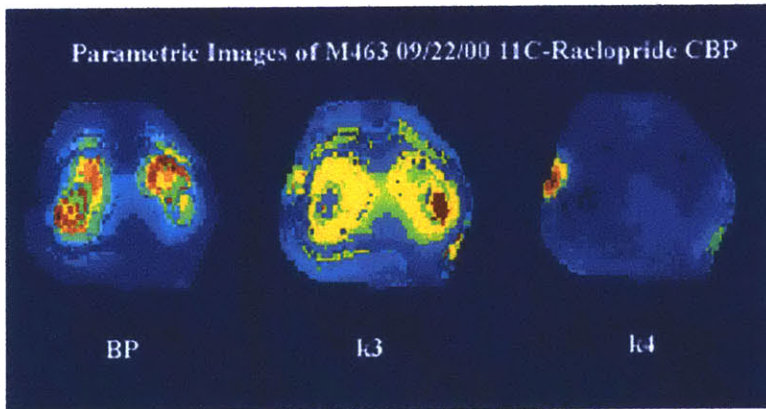


Figure 33. Parametric images of M463  $^{11}\text{C}$ -Raclopride, post MPTP treatment. Dynamic image sequence reconstructed by Hanning weighted convolution backprojection with a cutoff value of 0.8.

<b>Parametric Imaging of Binding Potential - <math>k_3/k_4</math></b>							
<b>CBP</b>							
	maximum value	left_caudate	right_caudate	left_putamen	right_putamen	left_striatum	right_striatum
<b><math>^{11}\text{C}</math>-raclopride</b>							
m458 post MPTP 053100	6.2924	3.966	3.654	5.067	5.942	4.179	4.456
m463 post MPTP 092200	6.2893	4.279	4.777	3.925	3.351	3.448	3.440
<b><math>^{11}\text{C}</math>-CFT</b>							
m458 pre MPTP 101599	6.2923	4.103	3.547	5.097	4.876	4.406	3.867
<b>MAP</b>							
	maximum value	left_caudate	right_caudate	left_putamen	right_putamen	left_striatum	right_striatum
<b><math>^{11}\text{C}</math>-raclopride</b>							
m458 pre MPTP 101599	6.2519	2.444	2.069	3.267	3.133	3.256	3.165
m458 post MPTP 053100	8.2918	5.370	5.615	5.717	5.729	5.876	5.449
m463 post MPTP 092200	7.1473	3.547	3.998	4.981	4.711	4.582	4.521
m281 pre MPTP 100598	7.438	4.167	3.721	4.701	4.462	4.434	4.091
<b><math>^{11}\text{C}</math>-CFT</b>							
m458 pre MPTP 101599	3.8371	3.100	3.136	3.305	3.293	2.961	2.948
m281 pre MPTP 100598	8.2918	6.415	6.1392	5.664	6.012	6.038	6.080

Table 12. Binding potential values ( $k_3/k_4$ ) obtained from parametric imaging.

## Chapter 7

### 7.1 Conclusions

Parametric imaging using the DIRECT algorithm and statistical reconstruction methods provides a new and powerful method for determining binding parameters in regions of interest. Used in parallel with traditional ROI analyses, the method provides an increased visualization of the physiological extent of degeneration or recovery. Small divergent areas in the tissue, such as transplanted tissue grafts, may be quantitated directly from the parametric image without partial volume effect. The results obtained from standard compartmental analyses in this work agree well with results derived from parametric imaging.

Statistical reconstruction methods that more accurately represent the physics of the imaging process provide an important complementary means for analyzing positron emission tomography data. Images reconstructed through these methods tend to possess lower bias; and, as the speed of computers increases, their use in physiological analyses can be explored more extensively for practical application.

Fusion of PET data with MRI provides another powerful means for analysis of physiological data, reducing operator guesswork and error in quantitation of PET images. Interpolation of serial slices and volumetric rendering from 2D PET images provides some differences in results when compared to an averaging of results from ROI analyses of 2D serial image data; however, volumetric quantitative analysis provides a more accurate method for determining regions of interest, extracting tracer counts, and applying these tracer counts to tracer-kinetic models for obtaining physiological parameters of interest. The method is more accurate because in principle it exploits the

use of anatomical information for use in the quantitation of PET images. Errors in quantitation can be more carefully attributed to coregistration errors. Operator error in drawing regions of interest is minimized. Furthermore, two-dimensional ROI analyses that do not employ the use of anatomical information enable analysis only in areas of high receptor density. The anatomical boundaries drawn on the image are sensitive to partial volume effects since the underlying tissue included within the slice thickness may have different receptor densities.

## **7.2 Future Work**

There are several directions for extending and evaluating the work presented in this thesis. First, a crossvalidation of MRI and PET coregistration must be performed to both validate the fusion of PET and MRI data and evaluate the quantitative results retrieved from the use of fused images. It would also be useful to analyze the effects of smoothing applied to the serial scans in the course of PET-MRI coregistration and volumetric rendering. Second, the effects of scatter and the partial volume effect must be evaluated. Third, data from Bayesian reconstruction algorithms must be further explored for routine use in physiological analysis. Finally, the parametric imaging algorithm used in this work should be compared with other parametric imaging algorithms, such as the basis function approach developed by Roger Gunn.

For PET-MRI crossvalidation several transformations can be applied to the high-resolution magnetic resonance images to generate simulated PET images so that the rigid body transformations between each magnetic resonance image and its associated simulated PET image are known. The estimation error of the coregistration in relation to the known transformation can then be used to evaluate the accuracy of the fusion

algorithms used under the assumption that the simulated PET data used embodies the essential features of actual PET data with respect to the coregistration.

## References

1. Wayne, Martin W. R., *Functional Imaging in Movement Disorders*, CRC Press LLC, 1990.
2. Brownell, A. L., Eidelberg, D., Dhawan, V., Isaacson, O., "Brain imaging as a diagnostic tool," *Encyclopedia of Life Sciences*, 2001.
3. Brownell, A. L., Jenkins, B. G., Elmaleh, D. R., Deacon, T. W., Spealman, R. D., Isaacson, O., "Combined PET/MRS brain studies show dynamic and long-term physiological changes in a primate model of Parkinson disease," *Nature Medicine*, Volume 4, Number 11, November 1998, pp. 1308-1312.
4. Koeppe, M. J., Gunn, R. N., Lawrence, A. D., Cunningham, V. J., Dagher, A., Jones, T., Brooks, D. J., Bench, C. J., Grasby, P. M., "Evidence for striatal dopamine release during a video game," *Nature*, Volume 393, May 1998, pp. 266-8.
5. Pifl, C., Schingnitz, G., Hornykiewicz, O., "The neurotoxin MPTP does not reproduce in the rhesus monkey the interregional pattern of striatal dopamine loss typical of human idiopathic Parkinson's disease," *Neuroscience Letters*, Volume 92, Number 2, October 1988, pp.228-33.
6. Brownell, A. L., Elmaleh, D. R., Meltzer, P. C., Shoup, T. M., Brownell, G. L., Fischman, A. J., Madras, B. K., "Cocaine Congeners as PET Imaging Probes for Dopamine Terminals," *The Journal of Nuclear Medicine*, Volume 37, Number 7, July 1996, pp.1186-1192.
7. Ehrin, E., Farde, L., de Paulis T., Eriksson L., Greitz T., Johnstrom P., Litton J. E., Nilsson J. L., Sedvall G., Stone-Elander S., et. al., "Preparation of <sup>11</sup>C-labelled Raclopride, a new potent dopamine receptor antagonist: preliminary PET studies of cerebral dopamine receptors in the monkey," *International Journal of Applied Radiation and Isotopes*, Volume 36, Number 4, April 1985, pp. 269-73.
8. Brownell, G. L., Burnham, C. A., Stearns, C. W., Chesler, D. A., Brownell, A. L., Palmer, M. R., "Developments in High-Resolution Positron Emission Tomography at MGH," *International Journal of Imaging Systems and Technology*, Volume 1, 1989, pp. 207-217.
9. Cherry, S. R., Dahlbom, M., Hoffman, E. J., "3D PET using a conventional multislice tomograph without septa," *Journal of Computer Assisted Tomography*, Volume 15, 1991, pp. 655-668.

10. Bailey, D. L., Meikle, S. R., "A Convolution-Subtraction scatter correction method for 3D PET," *Physics in Medicine and Biology*, Volume 39, 1994, pp. 411-424.
11. Levin, C. S., Dahlbom, M., Hoffman, E. J., "A Monte-Carlo Correction for the Effect of Compton Scattering in 3-D PET Brain Imaging," *IEEE Transactions in Nuclear Science*, Volume 42, Number 4, 1995, pp. 1181-1185.
12. Cherry, S. R., Meikle, S. R., Hoffman, E. J., "Correction and Characterization of Scattered Events in Three-Dimensional PET Using Scanners with Retractable Septa," *Journal of Nuclear Medicine*, Volume 34, 1993, pp. 671-678.
13. Shao, L., Freifelder, R., Karp, J. S., "Triple Energy Window Scatter Correction Technique in PET," *IEEE Transactions in Medical Imaging*, Volume 13, Number 4, 1994, pp.641-648.
14. Hoffman, E. J., Huang, S. C., Phelps, M. E., "Quantitation in positron emission computed tomography. 1 – Effect of object size," *Journal of Computer Assisted Tomography*, Volume 3, 1979, pp.299-308.
15. Jain, A., *Fundamentals of Digital Image Processing*, Prentice Hall International, Englewood Cliffs, NJ, 1989.
16. Bouman, C. A., Sauer, K., "A Unified Approach to Statistical Tomography Using Coordinate Descent Optimization," *IEEE Transactions on Image Processing*, Volume 5, Number 3, March 1996, pp. 480-492.
17. Frese, T., *Multiresolution Image Modeling and Bayesian Reconstruction Algorithms with Applications to Emission Tomography*, Ph.D. Thesis, Purdue University, May 2001.
18. West, J., Fitzpatrick, M. J., Wang, M. Y., Dawant, B. M., Maurer, C. R., Kessler, R. M., Maciunas, R. J., Barillot, C., Lemoine, D., Collignon, A., Maes, F., Suetens, P. Vandermeulen, D., vanden Elsen, P. A., Napel, S., Sumanaweera, T. S., Harkness, B., Hemler, P. F., Hill, D. L. G., Hawkes, D. J., Studholme, C., Maintz, J. B. A., Viergever, M. A., Malandain, G., Penec, X., Noz, M. E., Maguire, G. Q., Pollack, M., Pelizzari, C. A., Robb, R. A., Hanson, D., Woods, R. P., "Comparison and Evaluation of Retrospective Intermodality Brain Image Registration Techniques," *Journal of Computer Assisted Tomography*, Volume 21, Number 4, 1997, pp. 554-566.
19. Wells, W. M., Viola, P., Atsumi, H., Nakajima, S., Kikinis, R., "Multi-Modal Volume Registration by Maximization of Mutual Information," *Medical Image Analysis*, Oxford University Press.

20. Jacquez, J. A., Simon, C. P., "Qualitative Theory of Compartmental Systems," SIAM Review, Volume 35, Number 1, March 1993, pp.43-79.
21. Wayne, Martin W. R., Functional Imaging in Movement Disorders, Chapters 3 and 4, CRC Press LLC, 1990.
22. Golish, S. R., Hove, J. D., Schelbert, H. R., Gambhir, S. S., "A Fast Nonlinear Method for Parametric Imaging of Myocardial Perfusion by Dynamic  $^{13}\text{N}$ -Ammonia PET," The Journal of Nuclear Medicine, Volume 42, Number 6, June 2001, pp.924-931.
23. Gunn, R. N., Lammertsma, A. A., Hume, S. P., Cunningham, V. J., "Parametric Imaging of Ligand-Receptor Binding in PET Using a Simplified Reference Region Model," Neuroimage, Volume 6, 1997, pp. 279-287.
24. Bloomquist, G., Pauli, S., Farde, L., Ericksson, L, Persson, A., Halldin, C., "Dynamic models of reversible ligand binding," Clinical Research and Clinical Diagnosis (C. Beckers, A. Goffinet, A. Bol, Editors), Kluwer Academic Publishers, 1989.
25. Cunningham, V. J., Hume, S. P., Price, G. R., Ahler, R. G., Cremer, J. E., Jones, A. K. P., "Compartmental analysis of diprenorphine binding to opiate receptors in the rat in vivo and its comparisons with equilibrium data in vitro," Journal of Cerebral Blood Flow and Metabolism, Volume 11, 1991, pp.1-9.
26. Jones, D. R., Perttunen, C. D., Stuckman, B. E., "Lipchitzian Optimization Without the Lipschitz Constant," Journal of Optimization Theory and Application, Volume 79, Number 1, October 1993, pp. 157-181.
27. Watson, L. T., Baker, C. A., "A Fully Distributed Parallel Global Search Algorithm," Technical Report TR-00-06, Virginia Tech, Computer Science Department, 2000.
28. Gablonsky, J. M, "Modifications of the DIRECT Algorithm, Ph. D. Thesis, North Carolina State University, 2001.